Advanced Geodynamics: Fourier Transform Methods

David T. Sandwell

January 13, 2021

To Susan, Katie, Melissa, Nick, and Cassie

Eddie Would Go

Preprint for publication by Cambridge University Press, October 16, 2020

Contents

Introduction

Geodynamics by *Turcotte and Schubert* (2014) provides a deterministic, physics-based exposition of solid-Earth processes at a mathematical level assessible to most students. This classic textbook begins with a clear and concise overview of plate tectonics, followed by stress and strain in solids, elasticity and flexure, heat transfer, gravity, fluid mechanics, rock rheology, faulting, flows in porous media, and chemical geodynamics; the latest edition has sections on numerical modeling. I have used this textbook in a graduate level class for the past 28 years to prepare students in quantitative modeling of Earth processes. The book uses a minimum of mathematical complexity, so it can be understood by a wide range of students in a variety of fields. However, this more limited mathematical approach does not provide the graduate student with the tools to develop more advanced models having 3-dimensional geometries and time dependence.

This new book, *Advanced Geodynamics*, was developed to augment *Geodynamics* with more complex and foundational mathematical methods and approaches. The main new tool is multi-dimensional Fourier analysis for solving linear partial differential equations. Each chapter has a set of homework problems that make use of the higher-level mathematical and numerical methods. These are intended to augment the already excellent homework problems provided in *Geodynamics*. Detailed solutions are available from the author on request.

Chapter 1 - Observations Related to Plate Tectonics
This chapter reviews the global observations that were used to develop and refine the theory of plate tectonics. These include the latest maps of topography, marine gravity, seismicity, seafloor age, crustal thickness, and lithospheric thickness. This chapter also provides the global grids as overlays to Google Earth for exploration and interaction by students. In addition, all the data and tools needed to prepare the global maps using Generic Mapping Tools (GMT) is provided at the Cambridge web site.

Chapter 2 - Fourier Transform Methods in Geophysics
This chapter provides a brief overview of Fourier transforms and their properties including: similarity, shift, derivative, and convolution as well as the Cauchy residue theorem for calculating inverse transforms. These tools are used throughout the book

to solve multi-dimensional linear partial differential equations (PDE). Some examples include: Poisson's equation for problems in gravity and magnetics; the biharmonic equation for problems in linear viscoelasticity, flexure, and postglacial rebound; and the diffusion equation for problems in heat conduction. There are two approaches to solving this class of problem. In some cases, one can derive a fully analytic solution, or Green's function, to the point-source problem. Then a more general model is constructed by convolution using the actual distribution of sources. We focus on the second semi-analytic approach since it can be used to solve more complicated problems where the development of a fully analytic Green's function is impossible. This involves using the derivative property of the Fourier transform to reduce the PDE and boundary conditions to algebraic equations that can be solved in the transform domain. A more general model can then be constructed by taking the Fourier transform of the source, multiplying by the transform domain solution, and performing the inverse transform numerically. When dealing with spatially complex models, the second approach can be orders of magnitude more computationally efficient, because of the efficiency of the fast Fourier transform algorithm.

Chapter 3 Plate Kinematics
This chapter is focused on the basics of plate kinematics and relative plate motions. Students are encouraged to learn the names of the major plates, the plate boundaries, and triple junctions. We then review the rules governing the relative motions across the three types of plate boundaries, spreading ridges, transform faults, and subduction zones and use these rules for triple junction closure of the relative velocity vectors. The remainder of the chapter is concerned with plate motions on a sphere using vector calculus. The exercises involve calculations of plate motions and plate circuit closure using published rotation poles.

Chapter 4 Marine Magnetic Anomalies
This chapter uses the Fourier transform tools developed in chapter 2 to compute the scalar magnetic field that is recorded by a magnetometer towed behind a ship, given a magnetic timescale, a spreading rate, and a skewness. We first review the origin of natural remnant magnetism, to illustrate that the magnetized layer is thin compared with its horizontal dimension. Then the relevant differential equations are developed and solved under the ideal case of seafloor spreading at the north magnetic pole. Anomalies that formed at lower latitudes have a skewness that causes a wavelength-dependent phase shift. The exercises include the calculation of the magnetic anomalies associated with seafloor magnetic stripes and comparisons with shipboard magnetic data to establish the seafloor spreading rate and skewness.

Chapter 5 Cooling of the Oceanic Lithosphere
This chapter uses the Fourier transform method to solve for the temperature in the cooling oceanic lithosphere for half space and plate cooling models. For researchers in the areas of marine geology and geophysics, this is the essence of geodynamics since it explains the age variations of marine heat flow, seafloor depth, elastic thickness, and geoid height. The cooling models are also used to calculate the driving forces of plate motions including ridge push and slab pull. We focus on the buoyancy of the

lithosphere as a function of crustal thickness to explain the conditions when subduction is possible. A highlight of this chapter are 9 challenging heat flow exercises based on publications including thermal evolution of an oceanic fracture zone, lithospheric reheating from a mantle plume, and frictional heating during an earthquake.

Chapter 6 A Brief Review of Elasticity
This chapter reviews stress, strain, and elasticity in three dimensions using tensors. There is a brief presentation of tensor rotations, principal stress, and stress invariants. The principal stress vs. strain is inverted using the symbolic algebra in MATLAB . This is used to translate the Lame' elastic constants to Poisson's ratio and Young's modulus. The plane stress formulation is used to develop the moment versus curvature relationship for a thin elastic plate. This chapter is intended as a review and reminds some students that they need to master this material.

Chapter 7 - Crustal Structure, Isostasy, Swell Push Force, and Rheology
This chapter covers four topics. The first is basic structure of the oceanic and continental crust. The second and third topics are the vertical and horizontal force balances due to variations in crustal thickness. The vertical force balance, isostasy, provides a remarkably accurate description of variations in crustal thickness based on a knowledge of the topography. The horizontal force balance provides a lower bound on the force needed to maintain topographic variations on the Earth. The fourth topic is the rheology of the lithosphere. How does the lithosphere strain in response to applied deviatoric stress? The uppermost part of the lithosphere is cold, so frictional sliding along optimally-oriented, pre-existing faults governs the strength. At greater depth, the rocks can yield by nonlinear flow mechanisms. The overall strength-versus-depth profile is called the yield-strength envelope (YSE). The integrated yield strength transmits the global plate tectonic stress. Moreover, the driving forces of plate tectonics cannot exceed the integrated lithospheric strength. This provides an important constraint on the geodynamics of oceans and continents.

Chapter 8 Flexure of the Lithosphere
This chapter covers lithospheric flexure theory for an arbitrary vertical load. The approach is similar to the solutions of the marine magnetic anomaly problem, the lithospheric heat conduction problem, the strike-slip fault problem, and the flat-Earth gravity problem. In all these cases, we use the Cauchy residue theorem to perform the inverse Fourier transform. In a later chapter we combine this flexure solution with the gravity solution to develop the gravity-to-topography transfer function. Moreover, one can take this approach further, to develop a Green's function relating temperature, heat flow, topography, and gravity to a point heat source. In addition to the constant flexural rigidity solution found in the literature, we develop an iterative solution to flexure with spatially variable rigidity.

Chapter 9 Flexure Examples
This chapter provides practical examples of flexural models applied to structures in the lithospheres of Earth and Venus. The models are all solutions to the thin and thick-plate flexure equation, with a variety of surface loads, sub-surface loads, and boundary

conditions. Both gravity and topography data are used to constrain the models. We provide a numerical example that takes arbitrary topography and gravity anywhere on the Earth and uses Generic Mapping Tools to find the best elastic thickness and densities. A unique feature of this chapter is a comprehensive discussion of the non-linear relationship between plate bending moment and curvature that dominates at all subduction zones. This chapter includes 8 challenging flexure exercises based on publications including: ice shelf flexure, seamount flexure, fracture zone flexure, trench and outer rise yield strength and fracturing, and flexure on Venus.

Chapter 10 - Elastic Solutions for Strike-Slip Faulting
This chapter provides the mathematical development for the deformation and strain pattern due to a strike-slip fault in an elastic half space. We develop the solution from first principles using the Fourier transform approach. This approach does not explicitly use dislocations but simulates dislocations using body force couples following *Steketee* (1958) and *Burridge and Knopoff* (1964). The main advantage of this method is it is easily extended to three dimensions as well as complicated fault geometries. We also demonstrate the inherent non-uniqueness of inverting for slip versus depth from surface geodetic data yet show that the overall seismic moment is well resolved by surface data. The exercises at the end of the chapter illustrate the use of the 3-D Fourier transform, the Cauchy residue theorem, and computer algebra to solve for the response of an elastic half space to 3-D vector body forces.

Chapter 11 Heat Flow Paradox
This chapter is a quantitative investigation of the heat flow paradox that relates the expected frictional heating on a fault to the measurements of surface heat flow above the fault (e.g., *Lachenbruch and Sass* (1980)). A straightforward calculation, using a reasonable coefficient of friction, predicts measurably high heat flow above the fault that is not observed. We also investigate the maximum tectonic moment that could be sustained by a fault and show it is at least an order of magnitude greater than what is observed. Finally, we discuss the implications in terms of fault strength and earthquake predictability.

Chapters 12 The Gravity Field of the Earth, Part 1
This chapter provides a brief introduction to physical geodesy that describes the size and shape of the Earth and its gravity field. We decompose the Earth's reference gravity field into a spherical term and terms related to hydrostatic flattening by rotation. Superimposed on this reference model are anomalies discussed in later chapters. This chapter also describes how the reference Earth model has been developed and defined using satellite observations.

Chapters 13 Reference Earth Model: WGS84
This chapter is a summary of the reference shape and gravity field of the Earth as defined by the WGS84 parameters. Deviations from this reference model are defined in terms of geoid height, gravity anomaly, and deflections of the vertical.

Chapter 14 Laplace's Equation on Spherical Coordinates
This chapter introduces spherical harmonics and their properties for representing planetary gravity fields. We explain how the harmonic decomposition of a function on a sphere is analogous to the Fourier series decomposition of a 2-D function in Cartesian coordinates. We then use this spherical harmonic formulation to solve Laplace's equation and discuss upward continuation. Finally, we describe how the Earth's gravity field is represented as spherical harmonic coefficients and their time variation.

Chapter 15 - Laplace's Equation in Cartesian Coordinates and Satellite Altimetry
This chapter is focused on shorter wavelength components of the gravity field that are best represented in Cartesian coordinates using Fourier series. The Fourier transform of Laplace's equation is used to illustrate upward continuation as well as the connection between the anomalous potential (geoid height), its first derivatives (gravity anomaly and deflections of the vertical), and the second derivatives (gravity gradient tensor). This chapter also contains a rather complete discussion of satellite radar altimetry and how it is used to recover short wavelength variations in gravity which provides an important tool for investigating plate tectonics.

Chapter 16 - Poisson's Equation in Cartesian Coordinates
This chapter is focused on solving Poisson's equation using Fourier transforms. This solution is used to generate models of the disturbing potential and its derivatives from a 3-D density model. One approach is to perform a convolution of the Green's function with the 3-D density model. However, this approach, which appears in most textbooks, is error prone, computationally inefficient, and almost never used in modern publications. Instead, we illustrate the Fourier transform approach where the model is divided into layers and the density of each layer is Fourier transformed, upward continued, and summed to generate a surface model. A uniform density leads to the Bouguer slab correction. Finally, we develop Parkers exact formula for computing the gravity model for a layer with non-uniform topography.

Chapter 17 - Gravity/Topography Transfer Function and Isostatic Geoid Anomalies
This chapter combines thin-elastic plate flexure theory with the solution to Poisson's equation, to develop a linear relationship between gravity and topography. We discuss three uses of this relationship: 1) If both the topography and gravity are measured over an area that is several times greater than the flexural wavelength, then the gravity/topography relationship (in the wavenumber domain) can be used to estimate the elastic thickness of the lithosphere and/or the crustal thickness. 2) At wavelengths greater than the flexural wavelength, where features are isostatically-compensated, the geoid/topography ratio can be used to estimate the depth of compensation of crustal plateaus and hot-spot swells. 3) If the gravity field is known over a large area, but there is rather sparse ship-track coverage, the topography/gravity transfer function can be used to interpolate the seafloor depth between the sparse ship soundings. Finally, we show that the geoid height for isostatically-compensated topography is proportional to the swell-push or ridge-push force so under ideal conditions, one component of the plate driving force can be measured from the geoid height.

Chapter 18 Postglacial Rebound
This chapter considers the classic postglacial rebound problem using the Fourier transform approach. This chapter relies on chapter 6 in *Geodynamics* where the differential equations for viscous flow of an incompressible fluid are developed. We then solve for the response of a viscous half space to an arbitrary initial topography to illustrate the effect of load wavelength on the relaxation time. In addition, an elastic lithosphere is added to the viscous half space to simulate the present-day collapse of the flexural forebulge on the perimeter of the major Laurentide and Fennoscandia ice loads.

Chapter 19 - Driving Forces of Plate Tectonics
This chapter discusses the three major driving forces of plate motion ridge push, slab pull, and viscous drag. In previous chapters we showed that the ridge-push force is proportional to the age of the cooling ocean lithosphere. In this chapter we focus on the slab pull force which depends on age of the subducted lithosphere as well as the depth that the slab remains coupled to the surface. We use results from recent publications to calculate the positive and negative buoyancy of three major phase changes. 1) The basalt crust and depleted layer undergoe a phase change to the higher density eclogite. 2) Endothermic phase changes (positive Clapeyron slope) produce a zone of increased density in the cold lithosphere for a large part of the transition zone between depths of 310 km and 660 km. 3) Exothermic phase changes (negative Claperyon slope) below 660 km result in a zone of decreased density between depths of 660 and 720 km. Finally, we discuss the magnitudes of the forces for subduction of a small young plate as well as a large old plate to illustrate that the slab pull force (thermal plus phase changes) dominates ridge push and the difference must be attributed to the drag force.

The mathematical developments refer back to the section or equation in *Geodynamics* where the solutions are provided. Note that *Geodynamics* contains much more information than is provided in this new book *Advanced Geodynamics*, so both will be needed for a graduate-level geodynamics course.

Acknowledgements I thank Jerry Schubert, Tony Watts, Paul Wessel, and numerous students for reviewing and commenting on the manuscript. The Generic Mapping Tools (GMT) (*Wessel et al.*, 2019) were used extensively in data analysis and to generate figures. The individual chapters in this book were first developed as lecture notes and converted to LaTeX by the people at Dangerous Curve (typesetting@dangerouscurve.org), some of who have been doing typography since 1979.

Chapter 1

Observations Related to Plate Tectonics

1.1 Global Maps

The plate tectonic model states that the outer shell (lithosphere) of the Earth is divided into a small number of nearly rigid plates which slide over the weak asthenosphere. The plates are the surface thermal boundary layer (TBL) of mantle convection and descending slabs are the primary active components of the convective system. Plate boundaries are generally narrow and are characterized by earthquakes and volcanoes.

It is useful to assess the global data sets that are most relevant to plate tectonics. Below are a series of global maps that help to confirm various aspects of plate tectonic theory. Plate boundaries are classified as ridges, transform faults, or subduction zones based on basic observations of topography (Figure 1.1 and Figure 1.9), gravity anomaly (Figure 1.2) and seismicity (Figure 1.3). Remarkably, the axes of nearly all seafloor spreading ridges lie at a depth of 2500–3000 m below sea level, which is the level of isostasy for a hot thin lithosphere. Depths gradually increase away from the ridges, because of cooling and thermal contraction, so old ocean basins are commonly 4500–5000 m deep. Fracture zones and aseismic ridges also show up on these maps. Global seismicity (magnitude >5.1, Figure 1.3) highlights the plate boundaries and reveals their tectonic style. Shallow normal-faulting earthquakes (<30 km deep) are common along slow-spreading ridges, but largely absent along faster-spreading ridges where the plates are too thin and weak to retain sufficient elastic energy to generate large earthquakes. Transform faults are characterized by relatively shallow (<30 km) strike-slip earthquakes and they are common along both fast and slow-spreading ridges. The deeper earthquakes (green and blue dots in Figure 1.3) occur only in subduction zones where sheets of seismicity (i.e., Benioff zones) are critical evidence that the relatively cold lithosphere is subducting back into the mantle. But even convergent boundaries are characterized by shallow extensional earthquakes on the ocean side of the trenches. Some regions (e.g., Africa, Asia, Western North America, and the Indian Ocean) have distributed earthquake activity, indicating broad deformational zones. Topography and seismicity provide strong evidence for tectonic activity, but little or no information on the rate of plate motion.

Marine magnetic anomalies, combined with relative plate motion directions based on satellite altimeter measurements of fracture-zone trends, have been used to construct a global age map (Figure 1.4) of the relatively young (<180 Myr) oceanic lithosphere. Finally, the distribution of off-ridge volcanoes that have been active during the Quaternary mainly occur directly behind trenches where wet subducting slabs reach asthenospheric depths and trigger back-arc volcanism (Figure 1.5). A few active volcanoes occur within the interiors of the plates and in diffuse extensional plate boundaries.

The geoid (Figure 1.6 shows little correlation at long wavelengths with surface tectonics, and primarily reflects mass anomalies deep in the mantle. It is expected that the dynamic topography—the topography not due to crustal and near-surface variations—and the stress-state of the lithosphere will also reflect deep density differences. Insofar as volcanoes correlate with high surface elevations and extensional stress, one expects correlation of volcanoes with deep mantle structure, even if there is no material transfer. These maps are available for viewing in Google Earth at the following site: `http://topex.ucsd.edu/geodynamics/tectonics.kmz`.

A global map of crustal thickness (Figure 1.7) and Figure 1.9), based on refraction seismology as well as receiver function analyses, shows the major contrast between oceanic and continental crust. Ocean crustal thickness is relatively uniform (6-7 km). In contrast, the crustal thickness under the continents is generally 30-40 km in areas where the topography is within a few hundred meters of sea level. Areas of high elevation such as the Andes Mountains, the Himalaya Mountains, and the Tibetan Plateau have much thicker crust. As discussed throughout the text, the lack of high-amplitude, long-wavelength gravity anomalies is evidence that these large-scale topographic variations are isostatically compensated - mostly by variations in crustal thickness.

The final map shows lithospheric thickness derived from surface wave tomography (Figure 1.8). Over the ocean, the thickness of the lithosphere increases with the age of the plates. The thickest oceanic lithosphere occurs along the western side of the North and South Atlantic basins as well as the Western Pacific. The lithosphere is very thick (> 150 km) beneath the continental cratons of South Africa, Australia, northern Eurasia, northeastern North America, eastern South America, Greenland, and East Antarctica. Thinner continental lithospher occurs in tectonically active areas. One prominent exception is Tibet and the mountain ranges of central Asia where there is active crustal shortening and underthrusting of the Indian plate beneath Tibet.

Acknowledgements The data provided in these figures represent decades of data collection by thousands of scientists. Figures were constructed using Generic Mapping Tools (GMT) (*Wessel and Smith*, 1995; *Wessel et al.*, 2019). All the global maps can be reconstructed or customized using the data and GMT scripts at the following site `http://topex.ucsd.edu/geodynamics/global_maps.tgz`.

1.2 Exercises

Exercise 1.1. Install Google Earth on your computer and download the global tectonic maps (`http://topex.ucsd.edu/geodynamics/tectonics.kmz`). Identify the following triple junctions and use the overlays to determine the type of deformation (R-ridge, F-transform fault, or T-trench) for each of the three boundaries. Do this for Mendocino, Galapagos, Chile, Bouvet, Azores, and Indian Ocean triple junctions.

Exercise 1.2. Sketch a topographic profile across the Atlantic Ocean following a tectonic flow line (i.e., perpendicular to isochrons). The profile should extend from the east coast of North America to the west coast of Africa. Label the major topographic features. Provide approximate depths for the major topographic features. Sketch a second profile that extends from the ridge axis to the coast of North America and also intersects the Island of Bermuda. What are some major differences between this profile and the first profile?

Exercise 1.3. Where is the youngest ocean floor? Where is the oldest ocean floor? What are their approximate ages?

Exercise 1.4. What types of earthquake focal mechanisms occur on the three main types of plate boundaries?

Exercise 1.5. Use the book *Geodynamics* (*Turcotte and Schubert*, 2014) to complete Table 1.1. Devise a thought experiment to measure each quantity. The experiments should be physically realistic, but not necessarily practical.

Example temperature: One could use a thermometer to measure temperature, but that depends on knowing the coefficient of thermal expansion. One could use the definitions of the freezing/boiling point of water to define temperatures of $0°C$ and $100°C$. Or one could use the Stefan-Boltzmann law to measure temperature by measuring radiation L from a black body at temperature T.

$$L = \sigma T^4 \tag{1.1}$$

where σ is the Stefan Boltzmann constant ($5.67 \times 10^8\ Wm^{2\circ}\ K^4$).

Parameter	**Symbol**	**Units**	**Typical Value and Quantity**
Temperature	T	$^\circ C$ or $^\circ K$	$100^\circ C$ is the boiling point of water at 1 atm. of pressure.
Thermal conductivity			
Heat capacity			
Density			
Coefficient of thermal expansion (volumetric)			
Acceleration of gravity			
Gravitational constant			
Young's Modulus			
Poisson's Ratio			
Shear modulus			
Bulk modulus			
Dynamic viscosity			

Table 1.1

Chapter 2

Fourier Transform Methods in Geophysics

2.1 Introduction

Fourier transforms are used in many areas of geophysics such as image processing, time series analysis, and antenna design. Here we focus on the use of Fourier transforms for solving linear partial differential equations (PDE). Some examples include: Poisson's equation for problems in gravity and magnetics; the biharmonic equation for problems in linear viscoelasticity; and the diffusion equation for problems in heat conduction. We do not treat the wave equation in this book, because there are already many excellent books on seismology. For each of these problems, we search for the Green's function that represents the response of the model to a point source. There are two approaches to solving this class of problem. In some cases, one can derive a fully analytic solution, or Green's function, to the point-source problem. Then a more general model can be constructed by convolving the actual distribution of sources with the Green's function. A familiar example is the case of constructing a gravity anomaly model given a 3-D density anomaly structure. The second semi-analytic approach can be used to solve more complicated problems where the development of a fully analytic Green's function is impossible. This involves using the derivative property of the Fourier transform to reduce the PDE and boundary conditions to algebraic equations that can be solved exactly in the transform domain. A more general model can be constructed by taking the Fourier transform of the source, multiplying by the transform domain solution, and performing the inverse transform numerically. Indeed, the only difference between the two methods is that in the first case, the final model is generated by direct convolution, while in the second case, the convolution theorem is used for model generation. When dealing with spatially complex models, the second approach

The finite size of the area leads to a discrete set of wavenumbers $k_x = m/L, k_y = n/W$, and a discrete set of Fourier coefficients F_n^m. In addition to the finite size of the area, geophysical data commonly have a characteristic sampling interval Δx and Δy. Note that $I = L/\Delta x$ is the number of points in the x-direction and $J = W/\Delta y$ is the number of points in the y-direction. The Nyquist wavenumbers are $k_x = 1/(2\Delta x)$ and $k_x = 1/(2\Delta x)$, so there is a finite set of Fourier coefficients $-I/2 < m < I/2$ and $-J/2 < n < J/2$. Recall the trapezoidal rule of integration

$$\begin{aligned} \int_0^L f(x)\,\mathrm{d}x &\cong \sum_{\mathrm{i}=0}^{I-1} f(x_\mathrm{i})\Delta x \quad \text{where } x_\mathrm{i} = \mathrm{i}\Delta x \\ \int_0^L f(x)\,\mathrm{d}x &\cong \frac{L}{I}\sum_{\mathrm{i}=0}^{I-1} f(x_\mathrm{i}). \end{aligned} \tag{2.48}$$

The discrete forward and inverse Fourier transform are

$$F_n^m = \frac{1}{IJ}\sum_{\mathrm{i}=0}^{I-1}\sum_{\mathrm{j}=0}^{J-1} f_\mathrm{i}^\mathrm{j} \exp\left[-i2\pi\left(\frac{m}{I}\mathrm{i} + \frac{n}{J}\mathrm{j}\right)\right]. \tag{2.49}$$

$$f_\mathrm{i}^\mathrm{j} = \sum_{n=-I/2}^{I/2-1}\sum_{m=-J/2}^{J/2-1} F_n^m \exp\left[i2\pi\left(\frac{\mathrm{i}}{I}m + \frac{\mathrm{j}}{J}n\right)\right]. \tag{2.50}$$

The summations for the forward and inverse discrete Fourier transforms are similar, so one can use the same computer code for both transforms. Sorry for the dual use of the letter 'i.' The italic 'i' in front of the 2π is $\sqrt{-1}$, whereas the non-italic 'i's are integers.

2.8 Exercises

Exercise 2.6. What is the Fourier transform of the following function? Show your work and simplify the result.

$$\Pi(x) = \begin{cases} 1 & |x| < 1/2 \\ 1/2 & |x| = 1/2 \\ 0 & \textit{otherwise} \end{cases} \tag{2.51}$$

Exercise 2.7. Use the convolution theorem to calculate the Fourier transform of the following. Show your work.

$$\Lambda(x) = \begin{cases} 1 - |x| & |x| \le 1 \\ 0 & |x| > 1 \end{cases} \tag{2.52}$$

Note $\Lambda = \Pi * \Pi$.

Exercise 2.8. Perform the following path integral on $|z| = 2$.

$$\oint \frac{z+2}{(z^2+1)}\,\mathrm{d}z \tag{2.53}$$

Exercise 2.9.

```
%
% 1)  Write a program to generate a cosine function
%     using 2048 points.  Generate exactly 32, or 64 cycles
%     of the function. Plot the results and add labels.
%
figure(1)
clf
nx=2048;
kc=64/nx;
x=0:nx-1;
%
%  generate the function
%
y=cos(2*pi*x*kc);
%
figure(1)
plot(x,y);
xlabel('x')
ylabel('cos(x)')
pause
%
% 2) Take the Fourier transform of the function that you made in problem 1.
%    Use fftshift to shift the zero frequency to the center of the spectrum.
%    Generate wavenumbers for the horizontal axis.
%    Take the inverse FFT.  Do you get what you started with? (don't
%    forget to undo the fftshift.)
%
figure(2)
subplot(5,1,1),plot(x,y);
xlabel('x')
ylabel('cos(x)')
%
%  generate the wavenumbers
%
k=-nx/2:nx/2-1;
%
cy=fftshift(fft(y));
subplot(5,1,2),plot(k,real(cy));
xlabel('k')
subplot(5,1,3),plot(k,imag(cy));
%
%  do the inverse FFT
%
yo=ifft(fftshift(cy));
subplot(5,1,4),plot(x,real(yo));
xlabel('x')
ylabel('cos(x)')
subplot(5,1,5),plot(x,real(y-yo));
xlabel('x')
ylabel('difference')
pause
%
% 3) Do problem 2 over using a sine function instead of a cosine function.
%
% 4) Show that the Fourier transform of a Gaussian function is a Gaussian function.
%    Plot the difference between the fft result and the exact function.
%    When you do this problem, it is best to make the Gaussian function an even function
%    of x just prior to computing the fft(). If you do this then the transformed
%    Gaussian will be real and even.  Also you will need to scale the transform by
```

```
%    the point spacing dx = L/nx.
%
clear
figure(3)
nx=2048;
L=20;
dx=L/nx;
a=1.;
x=a*(-nx/2:nx/2-1)*dx;
g=exp(-pi*x.*x);
subplot(4,1,1),plot(x,g);
axis([-4,4,-.5,1.1])
xlabel('x')
ylabel('Gaussian')
%
%  generate the wavenumbers
%
k=(-nx/2:nx/2-1)/L;
%
cg=fftshift(fft(fftshift(g)))*dx;
%
% 5) Use this Gaussian example to demonstrate the stretch property of Fourier transform.  The
%    results should be compared in the wavenumber domain.
%
%
% 6) Use this Gaussian function to illustrate the shift property of the Fourier transform.
%    The results should be displayed as a shifted Gaussian in the space domain.
%
%
% 7) Use the Gaussian function to demonstrate the derivative property of the Fourier
%    transform.  The analytic derivative of the Gaussian should be compared with the
%    Fourier derivative in the space domain.
%
```

Chapter 3

Plate Kinematics

(Reference: (*Fowler*, 1990, Chapter 2))

3.1 Plate Motions on a Flat Earth

Plate tectonic theory describes the motions of rigid plates on a spherical Earth. However, when considering the relative motions very close to the plate boundary or at a triple junction, it is appropriate to use a flat-Earth approximation. We'll begin with the flat-Earth case and then move on to the spherical case. Consider the two plates A and B, which have a subduction zone boundary between them, such as the Nazca and South American plates. In this analysis, all plate motions are relative, so one can either consider plate B as fixed or plate A as fixed, and draw the relative vector velocity between them—as shown in Figure 3.1.

Example 3.3. *Galapagos Triple Junction* Given the rotation vectors of the Cocos plate relative to the Pacific plate and the Pacific plate relative to the Nazca plate, calculate the spreading rate at 2°N, 260°E.

$$\begin{aligned}\boldsymbol{\omega}_{\mathrm{CP}} + \boldsymbol{\omega}_{\mathrm{NC}} + \boldsymbol{\omega}_{\mathrm{PN}} &= 0\\ \boldsymbol{\omega}_{\mathrm{NC}} &= -\boldsymbol{\omega}_{\mathrm{CP}} - \boldsymbol{\omega}_{\mathrm{PN}}\\ \mathbf{v}_{\mathrm{NC}} &= \boldsymbol{\omega}_{\mathrm{NC}} \times \mathbf{r}(\theta, \phi)\end{aligned}$$

$|\mathbf{v}|$ is the magnitude of the spreading rate

3.7 Hot Spots and Absolute Plate Motions

So far, we have only considered relative plate motions, because there was no way to tie the positions of the plates to the mantle. One method of making this connection and thus determining absolute plate motions is to assume that "hot spots" remain fixed with respect to the lower mantle.

A hot spot is an area of concentrated volcanic activity. There is a subset of hot spots that have the following characteristics:

1. They produce linear volcanic chains in the interiors of the plates.
2. The youngest volcanoes occur at one end of the volcanic chain, and there is a linear increase in age away from that end.
3. The chemistry of the erupted lavas is significantly different from lava erupted at mid-ocean ridges or island arcs.
4. Some hotspots are surrounded by a broad topographic swell about 1000 m above the surrounding ocean basin.

These features are consistent with a model where the plates are moving over a relatively fixed mantle plume. After identifying the linear volcanic chains associated with the mantle plumes, it has been shown that the relative motions among hot spots is about 10 times less than the relative plate motions.

3.8 Exercises

Exercise 3.1. Calculate the spreading rate at a point on the northern Mid-Atlantic Ridge (latitude 30, longitude 319).

Exercise 3.2. Calculate the slip rate along the San Andreas Fault in San Francisco (latitude 38, longitude -122.7). You will need to use tables from *DeMets et al.* (2010).

Exercise 3.3. Where is the fastest seafloor spreading ridge on the Earth? Use Table 3.1 to calculate the spreading rate at that location.

Exercise 3.4. The vector sum of relative plate velocities around a triple junction is zero:

$$\mathbf{v}_{BA} + \mathbf{v}_{CB} + \mathbf{v}_{AC} = 0 \qquad (3.15)$$

Show that the following is also true at a position $\mathbf{r}_o$:

$$\boldsymbol{\omega}_{BA} + \boldsymbol{\omega}_{CB} + \boldsymbol{\omega}_{AC} = 0 \qquad (3.16)$$

where the $\boldsymbol{\omega}$'s are the relative rotation poles on a sphere and $\mathbf{r}_o$ is not parallel to any of the $\boldsymbol{\omega}$'s.

Exercise 3.5. Use the Google Earth overlays of vertical gravity gradient and earthquake epicenters to sketch the geometry of the ridges and transform faults around the Galapagos triple junction. Given the spreading rate across the southern segment of the East Pacific Rise (EPR) of 120 mm/yr, calculate the spreading rates on the northern segment of the EPR and the Cocos ridge.

Chapter 4

Marine Magnetic Anomalies

4.1 Introduction

This chapter develops the equations needed to compute the scalar magnetic field that is recorded by a magnetometer towed behind a ship, given a magnetic timescale, a spreading rate, and a skewness (e.g., *Schouten* (1971); *Schouten and McCamy* (1972)). A number of assumptions are made to simplify the mathematics. The intent is to first review the origin of natural remnant magnetism (NRM), to illustrate that the magnetized layer is thin compared with its horizontal dimension. Then the relevant differential equations are developed and solved under the ideal case of seafloor spreading at the north magnetic pole. This development highlights the Fourier approach to the solution to linear partial differential equations. The same approach will be used to develop the Green's functions for heat flow, flexure, gravity, and elastic dislocation. For a more general development of the geomagnetic solution, see the paper by *Parker* (1973).

4.2 Crustal Magnetization at a Spreading Ridge

As magma is extruded at the ridge axis, its temperature falls below the Curie point, and the uppermost part of the crust becomes magnetized in the direction of the ambient magnetic field. Figure 4.1, from *Kent et al.* (1993), illustrates the current model of crustal generation. Partial melt that forms by pressure-release in the uppermost mantle (~40 km depth) percolates to a depth of about 2000 m beneath the ridge, where it accumulates to form a thin magma lens. Beneath the lens a mush-zone develops into a 3500 m thick gabbro layer, by some complicated ductile flow. Above the lens, sheeted dikes (~1400 m thick) are injected into the widening crack at the ridge axis. Part of magnetic field at the seafloor spreading ridge axis. Most of the thermoremnant magnetism (TRM) is recorded in the upper 1000 meters of the oceanic crust. If the thickness of the TRM layer was too great, then as the plate cooled while it moved off the spreading ridge axis, the positive and negative reversals would be juxtaposed in dipping vertical layers (Figure 4.3). This superposition would smear the pattern observed by a ship. If the seafloor temperature was above the Curie temperature, as it is on Venus, then no recording would be possible.

The second scale is related to ocean floor depth and thus the Earth filter. The external magnetic field is the derivative of the magnetization, which, as shown above, acts as a high-pass filter applied to the reversal pattern recorded in the crust. The magnetic field measured at the ocean surface will be naturally smooth (upward continuation), due to the distance from the seafloor to the sea surface; this is a low-pass filter. This smoothing depends exponentially on ocean depth, so for a wavelength of 2π times the mean ocean depth, the field amplitude will be attenuated by $1/e$, or 0.37, with respect to the value measured at the seafloor. The combined result of the derivative and the upward continuation is a band-pass filter with a peak response at a wavelength of 2π times the mean ocean depth, or about 25 km. Wavelengths that are shorter (<10 km) or much longer (>500 km) than this value will be undetectable at the ocean surface.

The third and fourth scales that must match are the reversal rate and the seafloor-spreading rate. Half-spreading rates on the Earth vary from 10 to 80 km per million years. Thus, for the magnetic anomalies to be most visible on the ocean surface, the reversal rate should be between 2.5 and 0.3 million years. It is astonishing that this is the typical reversal rate observed in sequences of lava flows on land!! While most ocean basins display clear reversal patterns, there was a period between 85 and 120 million years ago when the magnetic field polarity of the Earth remained positive, so the ocean surface anomaly is too far from the reversal boundaries to provide timing information. This area of seafloor is called the Cretaceous quiet zone; it is a problem area for accurate plate reconstructions.

The lucky convergence of length and time scales makes it very unlikely that magnetic anomalies due to crustal spreading will ever be observed on another planet.

4.7 Exercises

Exercise 4.1. Explain why magnetic lineations cannot be observed from a spacecraft orbiting the Earth at an altitude of 400 km.

Exercise 4.2. Explain why scalar magnetic anomalies are not observed at a N-S oriented spreading ridge located at the magnetic equator.

Exercise 4.3. Write a MATLAB program to generate marine magnetic anomaly versus distance from a spreading ridge axis. Use equation 4.27 relating the Fourier transform of the magnetic anomaly to the Fourier transform of the magnetic timescale. You will need a magnetic timescale and the start of a MATLAB program (`https://topex.ucsd.edu/pub/class/geodynamics/hw3`). Assume symmetric spreading about the ridge axis, constant spreading rate, and constant ocean depth.

Use the program and magnetic anomaly profiles across the Pacific-Antarctic Rise (NBP9707.xydm) and the Mid-Atlantic Ridge (a9321.xydm) to estimate the half-spreading rate at each of these ridges. You may need to vary the mean ocean depth and skewness to obtain good fits.

Describe some of the problems that you had fitting the data. Provide some estimates on the range of total spreading rate for each ridge.

Exercise 4.4. Explain how the global gridded data set EMAG2 was constructed (`https://www.ngdc.noaa.gov/geomag/emag2.html`). Download the grid as a geotiff file and extract a subgrid approximately 2000 km by 2000 km. Use the upward continuation formula $A(\mathbf{k}, z) = A(\mathbf{k}, 0)e^{-2\pi|\mathbf{k}|z}$ to calculate the magnetic field at an altitude of 450 km. Explain why satellite measurements of the magnetic field cannot be used to map ocean anomalies related to seafloor spreading.

Chapter 5

Cooling of the Oceanic Lithosphere and Ocean Floor Topography

5.1 Introduction

This chapter uses the Fourier transform method to solve for the temperature in the cooling oceanic lithosphere. For researchers in the areas of marine geology, marine geophysics, and geodynamics, this is the most important concept you can learn from this book. As noted in the original paper on the topic by *Turcotte and Oxburgh* (1967), convection of the mantle is primarily controlled by thin thermal boundary layers . The surface thermal boundary layer, or *oceanic lithosphere*, is the most important component of the convecting system, because it represents the greatest temperature gradient in the Earth. It also has a greater surface area than the second-most important thermal boundary layer, which is at the core-mantle boundary. As the lithosphere cools it becomes denser, the seafloor depth increases, and ultimately the lithosphere founders (*subduction*). This subduction process both drives the convective flow and efficiently quenches the mantle.

This chapter covers the same material as *Geodynamics* (*Turcotte and Schubert*, 2014, Sections 4-15 to 4-17). The main difference is the method of solution. Turcotte and Schubert solve the half-space cooling problem by using a similarity variable to reduce the time-dependent heat conduction equation from a partial differential equation to an ordinary differential equation that can be solved by integration. These notes provide an alternate solution to the problem by using the tools of Fourier analysis. Basically,

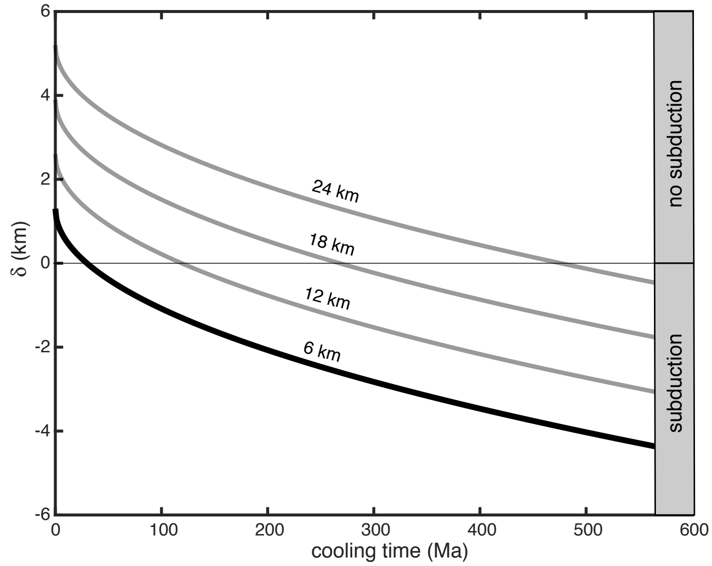

Figure 5.8: Total density defect thickness versus the age (or cooling time) of the lithosphere. Normal oceanic crust is 6 km thick and the lithosphere becomes negatively buoyant after cooling for 30 Ma. For a crustal thickness of 12 km, the time until negative buoyancy is delayed until 120 Ma. Lithosphere having a 24 km thick crust will remain buoyant for 500 Ma. Moreover, the lower lithosphere may be reheated or delaminate during this long time, so it may never subduct.

5.7 Exercises

Exercise 5.1. (a) What two measurements must be made to determine the conductive heat flow at the bottom of the ocean? (b) Why is it OK to measure heat flow in the upper few meters of sediment on the seafloor, while one needs a borehole hundreds of meters deep to obtain a reliable measure of heat flow on the continents?

Exercise 5.2. Assume the lithosphere of Venus has evolved to a steady-state temperature profile and there is no heat generated in the lithosphere. Given a current heat flow of $4 \times 10^{-2} W\mathrm{m}^{-2}$, a surface temperature of 450 C, a mantle temperature of 1500 C, and a thermal conductivity of 3.3 W $\mathrm{m}^{-1} C^{-1}$, calculate the thickness of the lithosphere.

Exercise 5.3. Solve for the temperature T as a function of time t and depth z in a cooling half space. The differential equation for heat diffusion is, and the boundary/initial conditions are

$$\begin{aligned}
\frac{\partial^2 T}{\partial z^2} &= \frac{1}{\kappa}\frac{\partial T}{\partial t} \\
T(0,t) &= T_o \\
T(\infty,t) &= T_m \\
T(z,0) &= T_m .
\end{aligned} \tag{5.68}$$

Use the following similarity variable $\eta = \frac{z}{2\sqrt{\kappa t}}$ to reduce the partial differential equation to an ordinary differential equation where κ is the thermal diffusivity, T_o is the surface temperature, and T_m is the initial temperature of the half space.

Exercise 5.4. Derive the following relationship between the rate of increase in seafloor depth with age $\frac{\partial d}{\partial t}$ and the difference between the surface and basal heat flow $(q_s - q_L)$.

$$\frac{\partial d}{\partial t} = \frac{\alpha}{C_p\left(\rho_m - \rho_w\right)}\left(q_s - q_L\right) \tag{5.69}$$

You will need Fourier's law, energy conservation, and isostasy as follows:

$$\begin{aligned}
q &= k\frac{\partial T}{\partial z} \\
\frac{\partial T}{\partial t} &= \frac{k}{\rho_m C_p}\frac{\partial^2 T}{\partial z^2} \\
d(t) &= \frac{-\alpha\rho_m}{(\rho_m - \rho_w)}\int_o^L T dz
\end{aligned} \tag{5.70}$$

where:

L	asymptotic lithospheric thickness and also the depth of compensation (m)
d	seafloor depth (m)
q	heat flow (W m^{-2})
α	coefficient of thermal expansion (C^{-1})
C_p	heat capacity (J kg^{-1})
ρ_w	seawater density (kg m^{-3})
ρ_m	mantle density (kg m^{-3})
k	thermal conductivity (W m^{-1}C^{-1})

Exercise 5.5. Calculate the cooling time for lithospheric subduction on Venus for crustal thicknesses of 16 km and 24 km. The surface temperature of Venus is 455 °C; use a deep-mantle temperature of 1400°C. Use Earth-like values of thermal expansion coefficient and thermal diffusivity in Table 5.2.

Exercise 5.6. Show that the coefficients of the Fourier series (5.55) are $a_n = \frac{2}{n\pi}$.

Exercise 5.7. Perform the integration in (5.62) to derive the formula for depth versus age given in (5.63).

Exercise 5.8. Seasonal variations in temperature near the surface of a glacier. Derive the formula 9.8 in Chapter 9 of *Cuffey and Patterson* (2010) and reproduce Figure 9.2. Also discuss the seasonal variations in heat flow.

Exercise 5.9. Temperature evolution of an oceanic fracture zone (*Sandwell and Schubert*, 1982a). An oceanic fracture zone is the boundary between lithosphere of different ages as shown in Figure 9.15. Consider the profile A-A' in Figure 9.15. The temperature far from the FZ near A is the deep mantle temperature T_m and far from the FZ on the A' side is the error function solution given in equation 5.23. As the FZ ages, there will be vertical diffusion of heat causing additional half-space cooling. Also there will be lateral heat transport across the FZ from the young (hot) side to old (cold) side. The differential equation, initial condition, and boundary conditions are

$$\frac{\partial^2 T}{\partial x^2} + \frac{\partial^2 T}{\partial z^2} = \frac{1}{\kappa}\frac{\partial T}{\partial t} \tag{5.71}$$

$$\begin{aligned} T(x,z,t_o) &= T_m & x < 0 \\ T(x,z,t_o) &= T_o + (T_m - T_o)\, erf\left(\frac{z}{\sqrt{\kappa t_o}}\right) & x > 0 \\ T(x,0,t_o) &= T_o & \\ T(x,z,t_o) &= T_m & \end{aligned} \tag{5.72}$$

where z is depth, x is distance across the FZ from A to A', t is the age of the A side and t_o is the age of the A' side. The solution for the temperture is (*Sandwell and Schubert*, 1982a)

$$T(x,z,t) = T_o + \frac{(T_m - T_o)}{2}\left[erfc\frac{x}{2\sqrt{\kappa(t-t_o)}}erf\frac{z}{2\sqrt{\kappa(t-t_o)}} + erfc\frac{-x}{2\sqrt{\kappa(t-t_o)}}erf\frac{z}{2\sqrt{\kappa t}}\right] \tag{5.73}$$

(a) Show this solution satisfies the differential equation, initial condition, and boundary conditions.

(b) Derive equation 5.73. This can be done by direct colvolution in the space domain or multiplication in the wavenumber domain. Both are algebraically challenging and cannot be found in the literature.

(c) Write a MATLAB program to create a contour plot or image of the temperature versus x and z for any time $t > t_o$

Exercise 5.10. Frictional heating during and earthquake. During an earthquake, most of the energy is converted to heat. Calculate the temperature across a fault during and following the earthquake for a variety of fault zone widths. Derive equation 5 in *Fialko* (2004).

Exercise 5.11. Temperature and heat flow from mantle plume. When the lithosphere passes over a mantle plume, the lower lithosphere is reheated. The motion of the lithosphere will advect the temperature anomaly $T(x, y, z)$ downstream. Also, heat will diffuse vertically through the lithosphere toward the surface, resulting in a heat flow anomaly that is maximum downstream from the source. To simulate this reheating, we setup a problem where a half space is moving at a velocity $\mathbf{v} = \left(v_x, v_y\right)$ through a fixed heat source at depth z_o given by $q_o(x, y, z) = q(x, y)\,\delta(z - z_o)$. The differential equation and boundary conditions for the temperature anomaly are

$$\mathbf{v} \cdot \nabla T - \kappa \nabla^2 T = \frac{q_o(x, y, z)}{\rho C_p} \tag{5.74}$$

$$\begin{aligned} &T(x, y, 0) = 0 \\ &\lim_{z \to \infty} T(x, y, z) = 0 \\ &\lim_{|x| \to \infty} T(x, y, z) = 0 \\ &\lim_{|y| \to \infty} T(x, y, z) = 0 \end{aligned} \tag{5.75}$$

where κ is the thermal diffusivity, C_p is the heat capacity, and ρ is the density. The solution for an arbitrary heat source at depth z_o is

$$T(\mathbf{k}, z) = \frac{Q(\mathbf{k})}{4\pi\rho C_p \kappa p}\left[e^{-2\pi p|z_o - z|} - e^{-2\pi p|z + z_o|}\right] \tag{5.76}$$

where $\mathbf{k} = \left(k_x, k_y\right)$ is the horizontal is the horizontal vector wavenumber and $Q(\mathbf{k})$ is the 2-D Fourier transform of the heat source. The parameter p in the solution is a combination of the wavenumbers and velocity

$$p^2 = \mathbf{k} \cdot \mathbf{k} - \frac{i}{2\pi\kappa}\mathbf{v} \cdot \mathbf{k} \tag{5.77}$$

(a) Derive equation 5.76. Start by taking the 3-D Fourier transform of equation 5.74 and separate the horizontal wavenumbers from the vertical wavenumber. The result is

$$\left(\mathbf{k}\cdot\mathbf{k}-\frac{i}{2\pi\kappa}\mathbf{v}\cdot\mathbf{k}+k_z^2\right)T\left(\mathbf{k},k_z\right)=\frac{Q\left(\mathbf{k}\right)e^{-i2\pi k_z z_o}}{4\pi^2\rho C_p\kappa} \tag{5.78}$$

Continue with the derivation using definition of p^2 given in equation 5.77. Perform the inverse transform with respect to k_z by integrating around the poles in the complex plane keeping only terms with decaying exponential in z. Finally use the method of images to satisfy the surface boundary condition.

(b) Compute the vertical heat flow and then the surface heat flow.

(c) Write a MATLAB program to compute the temperature and heat flow at any depth using a Gaussian heat source $q(x,y,z) = A\delta(z-z_o)\exp\left(-\frac{x^2+y^2}{2\sigma^2}\right)$ where σ is the half-radius of the source. The computational approach is to generate a 2-D array representing the Gaussian heat source. Put the center of the source somewhere in the middle of the 2-D array. Take its 2-D Fourier transform. Generate the wavenumbers and the solution in equation 5.76. Multiply the source and solution and perform the inverse 2-D transform. Note the equation for the temperature 5.76 is singular when both horizontal wavenumbers are zero (i.e., $p = 0$). Set this term to zero prior to computing the 2-D inverse Fourier transform. To simulate the Hawaiian plume, use an x-velocity of 40 mm/yr and a 2σ of 1000 km and place the source at a depth of 60 km. Make the width of the array 4000 km and the length of the array in the x-direction at least 20,000 km. This great length is needed to avoid the Fourier edge effect caused by heat flowing to great depth. Make images or contour maps of the temperature at a depth of 50 km and the surface heat flow making sure the pixels are square so the results are not distorted. Explore the parameter space of plume strength, A, plume radius σ, plume depth z_o, and plate speed v_x. Note if a finite thickness plate is used both the wrap-around and p-singulaity will be gone (*Sandwell*, 1982b). An example of the temperature and surface heat flow for a thinned lithosphere is shown in Figure 5.9.

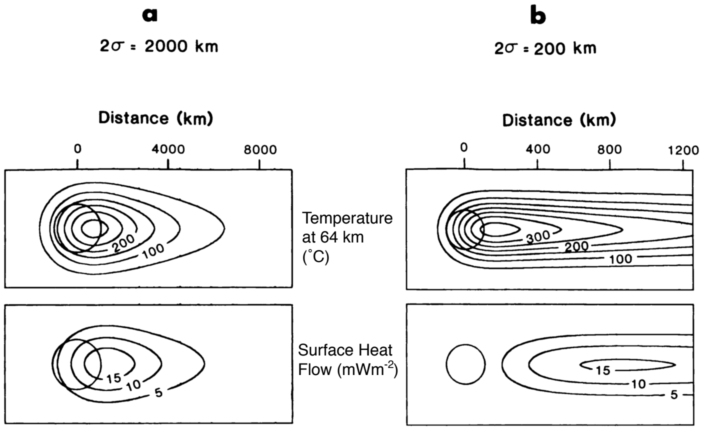

Figure 5.9: The response of the lithosphere moving at a velociy of 40 mm/yr over a Gaussian heat source with half widths (circles) of (a) 2000 km and (b) 200 km. The maximum temperature is approximately at the downstream edge of the source while the surface heat flow is displaced significantly downstream (*Sandwell*, 1982b).

Chapter 6

A Brief Review of Elasticity

This is a very brief review of the elasticity theory needed to understand the principles of stress, strain, and flexure in *Geodynamics* (*Turcotte and Schubert*, 2014). This review assumes that you have already taken a course in continuum mechanics. One difference from *Geodynamics* is that we follow the sign convention used by seismologists and engineers, where extensional strain and stress is positive.

6.1 Stress

Stress is a force acting on an area and is measured in Newtons per meter squared (N m^{-2}), which corresponds to a Pascal unit (Pa). Figure 6.1 shows a cube of solid material. Each face of the cube has three components of stress, so there are nine possible components of the stress tensor.

We will consider only the symmetric part of the stress tensor, so only six of these components are independent. The antisymmetric part of the tensor represents a torque. In Cartesian coordinates, the stress tensor is given by

$$\sigma_{ij} = \begin{bmatrix} \sigma_{xx} & \sigma_{xy} & \sigma_{xz} \\ \sigma_{xy} & \sigma_{yy} & \sigma_{yz} \\ \sigma_{xz} & \sigma_{yz} & \sigma_{zz} \end{bmatrix} \tag{6.1}$$

where index notation is the shorthand for dealing with tensors and vectors; a variable with a single subscript is a vector $\vec{a} = a_i$, a variable with two subscripts is a tensor $\boldsymbol{\sigma} = \sigma_{ij}$, and a repeated index indicates summation over the spatial coordinates. For

These equations are the starting point for the development of the relationship between bending moment and curvature provided in *Geodynamics* (*Turcotte and Schubert*, 2014, section 3.9).

6.6 Exercises

Exercise 6.3. Use the thin plate equations (equation (6.22)) to develop a linear relationship between moment and curvature. What are the important parameters that control the *flexural rigidity*? It will be helpful to study T&S (*Turcotte and Schubert*, 2014, section 3.9).

Chapter 7

Crustal Structure, Isostasy, Swell Push, and Rheology

7.1 Introduction

This chapter covers four topics. First the basic structure of the oceanic and continental crust is provided. The emphasis is on layer thickness and densities, and there is little discussion of composition. The second and third topics are the vertical and horizontal force balances due to variation in crustal thickness. The vertical force balance, *isostasy*, provides a remarkably accurate description of variations in crustal thickness based on a knowledge of the topography. The horizontal force balance provides a lower bound on the force needed to maintain topographic variations on the Earth. The basic question is: "What keeps mountain ranges from spreading laterally under their own weight?"

The fourth topic is the rheology of the lithosphere (*Brace and Kohlstedt*, 1980). How does the lithosphere strain in response to applied deviatoric stress? The uppermost part of the lithosphere is cold, so frictional sliding along optimally-oriented, pre-existing faults governs the strength. At greater depth, the rocks can yield by nonlinear flow mechanisms. The overall strength-versus-depth profile is called the *yield-strength envelope* (YSE). The integrated yield strength transmits the global plate tectonic stress. Moreover, the driving forces of plate tectonics cannot exceed the integrated lithospheric strength. This provides an important constraint on the geodynamics of oceans and continents.

The yield-strength-envelope formulation will also be used in the chapter on flexure. It provides an explanation for the increase in the thickness of the elastic layer as the lithosphere ages and cools. In addition, it is used to understand the depth of oceanic

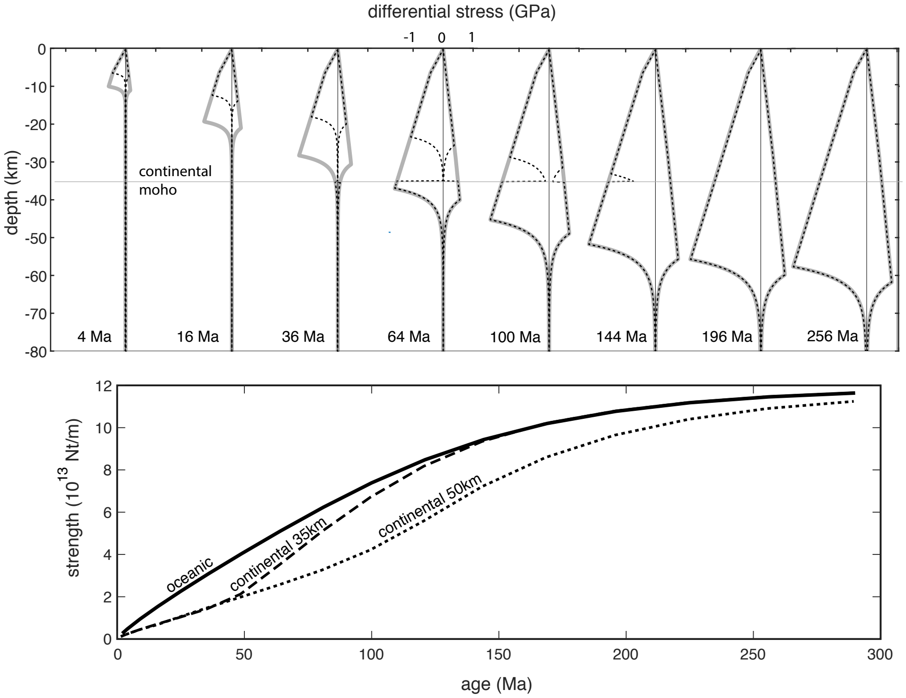

Figure 7.12: Oceanic (solid) and continental (dashed) yield strength envelope models as a function of cooling age based on the plate cooling model. (upper) Yield strength versus depth in extension (positive) and compression (negative). (lower) Integrated yield strength for oceanic (solid) and continental lithosphere having normal crustal thickness (dashed) and 50 km thick crust (short dash). Note that for the same geotherm, continental lithosphere is always weaker than oceanic lithosphere.

7.7 Exercises

Exercise 7.5. What is the average crustal stress needed to maintain the elevation of Tibet (5 km) with respect to the elevation of India (0 km – sea level). Use the crust and mantle densities of 2800 kg m^{-3} and 3200 kg m^{-3} , respectively. Assume the crustal thickness under India is 30 km.

(a) Use Airy isostasy to solve for the crustal thickness of Tibet.

(b) Calculate the outward driving force using equation (7.7).

(c) Calculate the average stress as the ratio of driving force to total crustal thickness.

Exercise 7.6. An ice sheet of thickness D and density $\rho_i = 960$ kg m^{-3} is floating on an ocean of density $\rho_w = 1025$ kg m^{-3} under the force of gravity g. Assume the ice sheet is thin relative to its horizontal dimensions. See Figure 7.13.

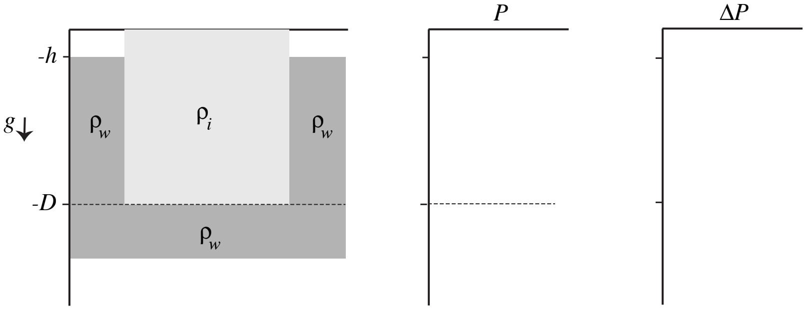

Figure 7.13

(a) Sketch the pressure versus depth for the ice and water, as well as the pressure difference versus depth.

(b) Derive an expression for the freeboard (i.e., height above sea level) of the ice sheet.

(c) Derive an expression for the outward driving force per unit length into the page caused by this density configuration

$$F_s = \int_{-D}^{0} \Delta P(z)\, \mathrm{d}z$$

Check your results in a limiting case.

Chapter 8

Flexure of the Lithosphere

This chapter is basically a supplement to *Geodynamics* (*Turcotte and Schubert*, 2014, Chapter 3). The results of the first derivation are the same as *Geodynamics* (*Turcotte and Schubert*, 2014, equation (3.130)), but rather than guessing the general solution, the solution is developed using Fourier transforms. The approach is similar to the solutions of the marine magnetic anomaly problem, the lithospheric heat conduction problem, the strike-slip fault flexure problem, and the flat-Earth gravity problem. In all these cases, we use the Cauchy integral theorem to perform the inverse Fourier transform. Later we'll combine this flexure solution with the gravity solution to develop the gravity-to-topography transfer function. Moreover, one can take this approach further, to develop a Green's function relating temperature, heat flow, topography, and gravity to a point heat source (e.g., *Sandwell* (1982a)). In addition to the constant flexural rigidity solution found in the literature, we develop an iterative solution to flexure with spatially variable rigidity.

Before going over these notes, please reread *Geodynamics* (*Turcotte and Schubert*, 2014, Section 3-9) on the development of moment versus curvature for a thin elastic plate.

The loading problem is illustrated in Figure 8.1. We start with a simple line source, but the solution method also applies to a point source. Of course, the point source Green's function can be convolved with an arbitrary load distribution to make the solution completely general; we'll do this later. The vertical force balance for flexure of a thin elastic plate floating on the mantle is described by the following differential equation

$$\underbrace{\frac{\mathrm{d}^2}{\mathrm{d}x^2}\left(D(x)\frac{\mathrm{d}^2 w}{\mathrm{d}x^2}\right)}_{\text{flexural resistance}} \quad + \quad \underbrace{F\frac{\mathrm{d}^2 w}{\mathrm{d}x^2}}_{\text{end load}} \quad + \quad \underbrace{\Delta\rho g w}_{\text{restoring force}} \quad = \quad \underbrace{q(x)}_{\text{vertical load}}\,. \tag{8.1}$$

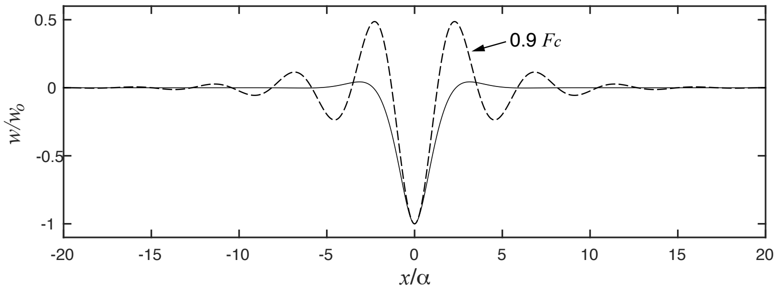

Figure 8.6: (solid) Normalized flexure of a continuous plate under a line load. (dashed) Normalized flexure with line load and end load. The plate begins to buckle at the flexural wavelength.

An example of the flexure due to a line load on a thin elastic plate is shown in Figure 8.6. When no end load is applied, the flexure follows the analytic solution for a continuous plate given in equation (8.13). When an end load is applied the plate begins to buckle. This example has an end load $F = 0.9F_c$.

Next, consider an example of buckling of oceanic lithosphere that is 50 km thick. The density contrast $\Delta\rho = (\rho_m - \rho_w)$ and other parameters are given in Table 8.1. The parameters of interest are the average stress at the ends of the plate $\sigma = F_c/h$ and the buckling wavelength λ_c. For this case, the values are 4.9 GPa and 475 km. From the analysis of the yield strength envelope, it is clear that this level of stress cannot be sustained by even the strongest oceanic lithosphere. Therefore, the elastic buckling model is not relevant for the Earth. One must consider the inelastic properties of the lithosphere to understand the response to large end loads.

8.4 Exercises

Exercise 8.1. Continental yield strength envelope model. The continental yield strength has been described as a jelly sandwich consisting of a weak layer (jelly) between two strong layers (bread). The flexural rigidity of a single strong layer is

$$D = \frac{Eh^3}{12\,(1-\nu^2)} \tag{8.31}$$

(a) What is the flexural rigidity of two strong layers, each of thickness $h/2$, that are not bonded along their common interface?

(b) What is the effective elastic thickness for this layered case (bottom diagram in Figure 8.7)?

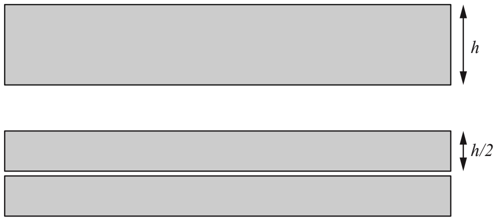

Figure 8.7: (solid) (top) Single plate of thickness h. (bottom) Two plates each of thickness $h/2$ are not bonded at their interface, so they act independently under a bending moment.

Exercise 8.2. Write a MATLAB program to generate the two flexure curves in Figure 8.6. Start with the code used in Exercise 2.9.

Exercise 8.3. (a) Consider an ice shelf of thickness h (150 m) and density ρ_i (980kgm^{-3}) floating on an ocean of density ρ_w (1025kgm^{-3}) . The ice starts at a cold uniform temperature of T_o (-22C) as it flows out onto the ocean and then is warmed at its base to a temperature of seawater T_w (-2C). The ice has enough time to equilibrate so the geotherm is approximately linear with depth and is

$$T(z) = (T_w - T_o)\frac{z}{h} + T_o. \tag{8.32}$$

Show that the thermal bending moment is

$$M_T = \frac{\gamma E (T_w - T_o)}{12} h^2 \ . \tag{8.33}$$

where E (1.6×10^{9}Pa) is Young's modulus and γ (5.5×10^{-5}C^{-1}) is the linear coefficient of thermal expansion. Assume that the depth-integrated end load is zero.

(b) Derive the following formula for the deflection of the plate as a function of distance from the edge of the ice shelf. Hint see equation 3.151 in Turcotte and Schubert.

$$w(x) = \frac{\alpha^2 M_T}{2D} e^{-(x/\alpha)} \left[\cos(x/\alpha) - \sin(x/\alpha)\right]. \tag{8.34}$$

c) Plot the deflection of the plate as a function of distance from the edge of the ice shelf. How does this compare with the topography of the rampart and moat shown in Figure 2 of *Scambos et al.* (2005).

Chapter 9

Flexure Examples

This chapter provides practical examples of flexural models applied to structures in the lithospheres of Earth and Venus. The models are all basically solutions to the thin-plate flexure equation, with a variety of surface loads, sub-surface loads, and boundary conditions. Both gravity and topography data are used to constrain the models. We'll see in a following chapter that gravity data provide important constraints on the topography of the Moho. Figures and captions from various sources are provided on the following pages. The excellent book by *Watts* (2001) provides a much more thorough and extensive survey of oceanic and continental flexures.

The features discussed below include:

Seamounts undersea volcanoes loading the oceanic lithosphere.

Trenches plate bending at subduction zones on Earth and Venus.

Fracture Zones flexure that accumulates due to the differential subsidence across an oceanic fracture zone.

In addition, there are seven exercises at the end of the chapter to explore a wider variety of published flexure models including ice shelves and rift flank uplifts. Students can select a topic of interest, reproduce the published results, and provide a critical analysis of each paper.

9.4 Exercises

Exercise 9.1. Show that Equation 9.2 is true by integrating the solution for the trench flexure case (*Geodynamics* (*Turcotte and Schubert*, 2014, Equation 3-142))

$$w(x) = w_o e^{-x/\alpha} \cos\frac{x}{\alpha} \ . \tag{9.4}$$

Compare this with the moment computed from the curvature

$$M(x) = D\frac{\partial^2 w}{\partial x^2} \ . \tag{9.5}$$

You will need the relationship between α and D given in Equation 8.6.

Exercise 9.2. Ice Shelf Flexure - Discuss the tidal flexure model and derive equation 3 in the paper by *Vaughan* (1995). Generate the curve shown in Figure 5. Explain the overall findings of the paper.

Exercise 9.3. Seamount Flexure - Discuss the seamount loading flexure model and derive equation 11 of *Banks et al.* (1977). How would one calculate a model for a load of arbitrary shape? Use GMT or matlab to generate the flexure for a Gaussian-shaped seamount.

Exercise 9.4. Trench Flexure - Discuss the trench flexure problem and derive the solution given in equation 2 of *Caldwell et al.* (1976). Reproduce the graphs shown in Figure 3. Explain the overall findings of the paper.

Exercise 9.5. Fracture Zone Flexure - Discuss the fracture zone flexure problem and derive the solution given in equation 11 of *Sandwell and Schubert* (1982a). Calculate the topography and stress across a single fracture zone with different flexural rigidities on either side (simple case, no time dependence, no lateral heat conduction). Explain the overall findings of the paper.

Exercise 9.6. Flexure on Venus - Discuss the Venus Flexure problem and why it is important. Derive equations 2 in *Johnson and Sandwell* (1994). Derive equation 10 from equations 7 and 8. When might it be more appropriate to use a ring load rather than a bar load. Explain the overall findings of the paper in terms of the geothermal gradient on Venus.

Exercise 9.7. Outer Rise Yield Strength - Discuss why it is important to consider the finite yield strength of the lithosphere when modeling flexure at subduction zones. Discuss equations 3 and 12 in *McNutt and Menard* (1982). Discuss the difference between the effective elastic thickness and the mechanical thickness.

Exercise 9.8. Rift Flank Uplift - Why do the flanks of rifts go up? Reproduce Figure 3 in *Brown and Phillips* (1999). Discuss the equation 11 and Figure 5 in *Weissel and Karner* (1989).

Exercise 9.9. Lake Loading - Discuss the lake loading flexure problem and its effect on the San Andreas Fault. Derive equations 2 and 3 in *Luttrell et al.* (2007). Reproduce the thin-plate plots in Figure 4. Explain the overall findings of the paper.

Chapter 10

Elastic Solutions for Strike-Slip Faulting

(References: (*Weertman and Weertman*, 1966; *Savage and Burford*, 1973; *Cohen*, 1999))

This chapter provides the mathematical development for the deformation and strain pattern due to an infinitely long, strike-slip fault in an elastic half space. The notes are similar to sections 8-6 through 8-9 in *Geodynamics* (*Turcotte and Schubert*, 2014). While we follow the overall theme of Chapter 8, we'll deviate in two respects. First we'll use a coordinate system with the z-axis pointed upward, to be consistent with the other chapters on gravity, magnetics, and heat flow. Second we'll develop the solution from first principles using the Fourier transform approach. This approach does not explicitly use dislocations (e.g., *Segall* (2010)) but simulates dislocations using body force couples following *Steketee* (1958) and *Burridge and Knopoff* (1964).

10.1 Interseismic Strain Buildup

The first objective is to derive an expression for the surface displacement $v(x)$ and surface strain $\delta v/\delta x$ for the model shown in Figure 10.1. A constant velocity V is applied at an elastic half space. There is a fault in the half space with locked and creeping sections.

displacement vector $\mathbf{u}(x, y, z)$ on the surface or inside of the Earth due to a vector body force at depth. This solution can be used to construct a variety of models such as fault slip of arbitrary complexity (e.g., *Smith and Sandwell* (2003)). We start with the equations that relate stress to body forces, stress to strain, and strain to displacement

$$\sigma_{ij,j} = -b_i \tag{10.57}$$

$$\sigma_{ij} = \delta_{ij}\lambda\varepsilon_{kk} + 2\mu\varepsilon_{ij} \tag{10.58}$$

$$\varepsilon_{ij} = \frac{1}{2}\left(u_{i,j} + u_{j,i}\right). \tag{10.59}$$

Substitute equation 10.59 into equation 10.58

$$\sigma_{ij} = \delta_{ij}\lambda u_{k,k} + \mu\left(u_{i,j} + u_{j,i}\right). \tag{10.60}$$

Substitute equation 10.60 into equation 10.57

$$\delta_{ij}\lambda u_{k,kj} + \mu\left(u_{i,jj} + u_{j,ij}\right) = -b_i \tag{10.61}$$

and rewrite as

$$(\lambda + \mu)\, u_{k,ki} + \mu u_{i,kk} = -b_i. \tag{10.62}$$

Equation 10.62 can be written as 3 partial differential equations

$$\begin{aligned}
\mu\nabla^2 u + (\lambda + \mu)\left[\tfrac{\partial^2 u}{\partial x^2} + \tfrac{\partial^2 v}{\partial y \partial x} + \tfrac{\partial^2 w}{\partial z \partial x}\right] &= -b_x \\
\mu\nabla^2 v + (\lambda + \mu)\left[\tfrac{\partial^2 u}{\partial x \partial y} + \tfrac{\partial^2 v}{\partial y^2} + \tfrac{\partial^2 w}{\partial z \partial y}\right] &= -b_y \\
\mu\nabla^2 w + (\lambda + \mu)\left[\tfrac{\partial^2 u}{\partial x \partial z} + \tfrac{\partial^2 v}{\partial y \partial z} + \tfrac{\partial^2 w}{\partial z^2}\right] &= -b_z
\end{aligned} \tag{10.63}$$

Next introduce a vector body force at $x = y = 0$, $z = a$. To satisfy the boundary condition of zero shear traction at the surface, an image source is also applied at $x = y = 0$, $z = -a$ (Figure 10.11). Equation 10.64 describes this point body force at the source and image locations, where $\mathbf{F} = \left(F_x, F_y, F_z\right)$ is a vector force with units of force.

$$\mathbf{b}(x, y, z) = \mathbf{F}\delta(x)\,\delta(y)\,\delta(z - a) + \mathbf{F}\delta(x)\,\delta(y)\,\delta(z + a) \tag{10.64}$$

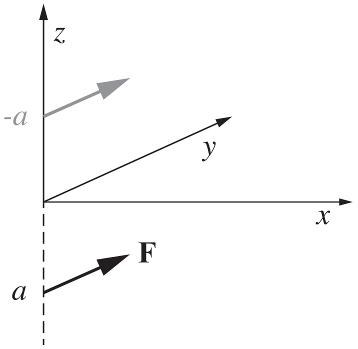

Figure 10.11: Coordinate system with point vector body forces at a and $-a$.

Exercise 10.1. It is left as an exercise to take the 3-D Fourier transform of equations 10.63 and 10.64 to reduce the partial differential equations to a set of linear algebraic equations. Several of the properties of Fourier transforms, given in Chapter 2, will be helpful. The result is

$$(\lambda+\mu)\begin{bmatrix} k_x^2+\frac{\mu\mathbf{k}^2}{(\lambda+\mu)} & k_yk_x & k_zk_x \\ k_xk_y & k_y^2+\frac{\mu\mathbf{k}^2}{(\lambda+\mu)} & k_zk_y \\ k_xk_z & k_yk_z & k_z^2+\frac{\mu\mathbf{k}^2}{(\lambda+\mu)} \end{bmatrix}\begin{bmatrix} U(\mathbf{k}) \\ V(\mathbf{k}) \\ W(\mathbf{k}) \end{bmatrix} = \frac{e^{-i2\pi k_z a}+e^{i2\pi k_z a}}{4\pi^2}\begin{bmatrix} F_x \\ F_y \\ F_z \end{bmatrix} \tag{10.65}$$

where $\mathbf{k}=\left(k_x,k_y,k_z\right)$ and $\mathbf{k}^2=\mathbf{k}\cdot\mathbf{k}$.

Exercise 10.2. Invert the linear system of equations to isolate the 3-D displacement vector solution for $U(\mathbf{k})$, $V(\mathbf{k})$, and $W(\mathbf{k})$. This can be done using the symbolic algebra capabilities of MATLAB or another computer algebra package.

$$\begin{bmatrix} U(\mathbf{k}) \\ V(\mathbf{k}) \\ W(\mathbf{k}) \end{bmatrix} = \frac{(\lambda+\mu)\left(e^{-i2\pi k_z a}+e^{i2\pi k_z a}\right)}{\mu(\lambda+2\mu)4\pi^2\mathbf{k}^4}\begin{bmatrix} \left(k_y^2+k_z^2\right)+\frac{\mu\mathbf{k}^2}{(\lambda+\mu)} & -k_yk_x & -k_zk_x \\ -k_xk_y & \left(k_x^2+k_z^2\right)+\frac{\mu\mathbf{k}^2}{(\lambda+\mu)} & -k_zk_y \\ -k_xk_z & -k_yk_z & \left(k_x^2+k_y^2\right)+\frac{\mu\mathbf{k}^2}{(\lambda+\mu)} \end{bmatrix}\begin{bmatrix} F_x \\ F_y \\ F_z \end{bmatrix} \tag{10.66}$$

One can check the inversion using the following MATLAB symbolic code.

```
%
```

```
%  MATLAB routine to check the solution in the kx, ky, kz domain.
%
    pi = sym(’pi’);
    kx=sym(’kx’);
    ky=sym(’ky’);
    kz=sym(’kz’);
% elastic constants
    la=sym(’la’);
    mu=sym(’mu’);
    lam=la+mu;
% combinations of wavenumbers
    c=sym(’c’);
    c=(kx*kx+ky*ky+kz*kz);
% forward matrix
    A=[kx*kx+mu*c/lam,ky*kx,  kz*kx;
       kx*ky,ky*ky+mu*c/lam,kz*ky;
       kx*kz,ky*kz,kz*kz+mu*c/lam];
% solution in Fourier domain, inverse matrix
    B=[c*mu/lam+ky*ky+kz*kz,-kx*ky,-kx*kz;
       -kx*ky,c*mu/lam+kx*kx+kz*kz,-kz*ky;
       -kx*kz,-ky*kz,  c*mu/lam+kx*kx+ky*ky];
% normalize
    A=A*lam;
    B=B*lam/(mu*(la+2*mu)*c*c);
% multiply to get the identity matrix
    C=B*A;
    simplify(C)
ans =

[ 1, 0, 0]
[ 0, 1, 0]
[ 0, 0, 1]
```

The next step is to perform the inverse Fourier transform with respect to k_z of each of the three terms for each of the three displacement component for both the source and the image. There are 12 different integrations to be performed although they are all very similar. For example, the following is the inverse transform for the $V(\mathbf{k})$ displacement driven by the F_x component of body force (source not image).

$$[V(\mathbf{k}_h, z) = -F_x \frac{(\lambda + u)}{\mu(\lambda + 2u)} \frac{k_x k_y}{4\pi^2} \int_{-\infty}^{\infty} \frac{e^{i2\pi k_z (z-a)}}{(k_z + i|\mathbf{k}_h|)^2 (k_z - i|\mathbf{k}_h|)^2} dk_z \qquad (10.67)$$

where $\mathbf{k}_h = \left(k_x, k_y\right)$ is the horizontal wavenumber and $|\mathbf{k}_h| = \left(k_x^2 + k_y^2\right)^{1/2}$. The denominator has four poles in the complex plane, two at $-i|\mathbf{k}_h|$ and two at $i|\mathbf{k}_h|$.

Exercise 10.3. Use the Cauchy residue theorem, for the case of repeated poles, and the boundary condition that the displacement must vanish as $z \to \infty$ to derive the $V(\mathbf{k})$ displacement.

$$V(\mathbf{k}_h, z) = -F_x \frac{(\lambda + u)}{\mu(\lambda + 2u)} \frac{k_x k_y}{2\pi} \left[\frac{1 + 2\pi |\mathbf{k}_h|}{4|\mathbf{k}_h|^3} \right] e^{-2\pi|\mathbf{k}_h|(z-a)} \tag{10.68}$$

There are a number of additional steps needed to develop a full algorithm for computing displacements due to double-couple fault sources. These are published in *Smith and Sandwell* (2003). The astute reader will notice that while the introduction of an image body force achieves the zero shear stress boundary condition, the normal stress at the surface is not zero. This boundary condition can be corrected by applying an equal but opposite vertical stress following *Steketee* (1958). Also, for purely vertical faults, the body force can be analytically integrated over depth. The final step is a numerical implementation for a complicated fault model. This involves making 2-D grids of each of the three components of the body force. The forces in these grids can be arranged to create single or double couples in an arbitrarily complex pattern. For a more complete description, see *Smith and Sandwell* (2003). These three force grids are Fourier transformed and multiplied by the elements of the Earth response (e.g., equation 10.68), The results are summed and inverse transformed to calculate the vector displacement as well as all the stress components through differentiation. The main advantages of this approach are computational efficiency and the ability to construct very complex fault systems. An example of the Coulomb stress accumulation rate on the San Andreas Fault system is shown in Figure 10.12 . Note this analysis was extended to include a uniform-thickness elastic plate over a viscoelastic half space (*Smith and Sandwell* (2004)). The computer code for creating these 3-D, time-dependent fault models can be found at: `https://github.com/dsandwell/fftfault`.

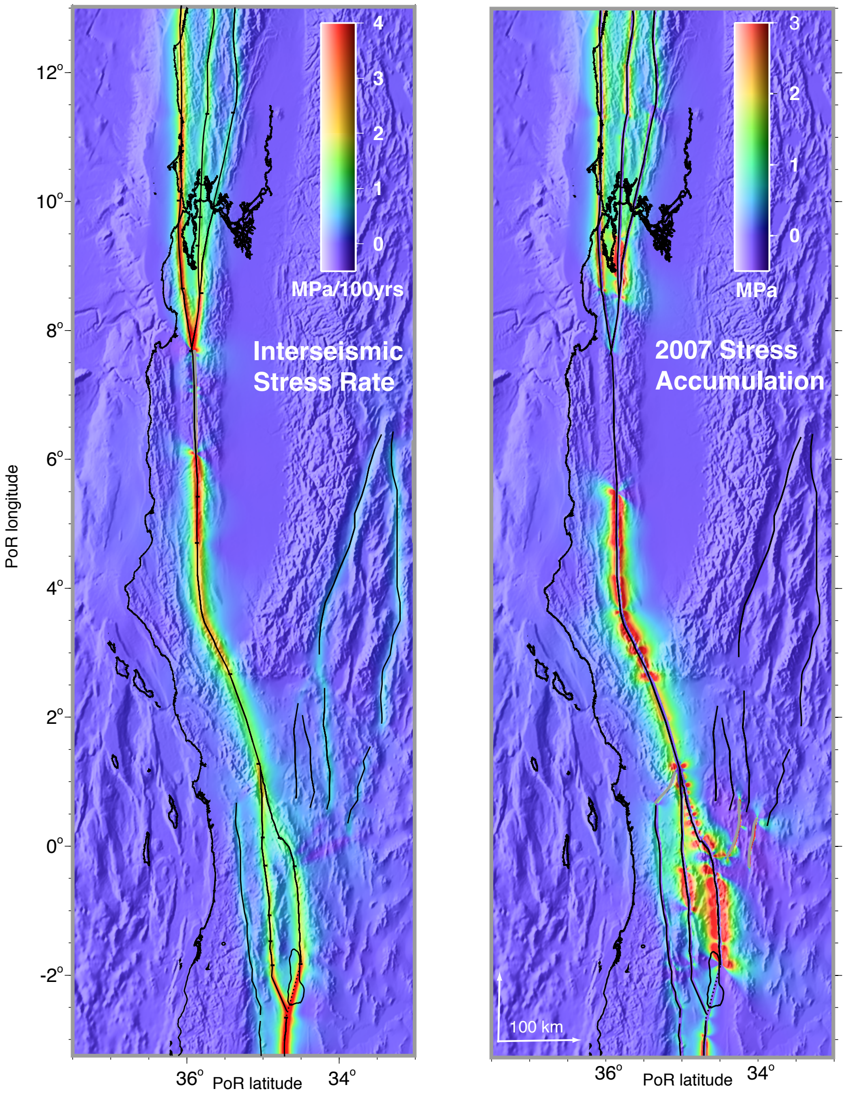

Figure 10.12: (left) Coulomb stress accumulation rate of the SAFS, evaluated at 1/2 of the locking depth projected into pole of rotation coordinate system (*Wdowinski et al.*, 2007). (right) Present-day (calendar year 2007) Coulomb stress accumulation based on stress accumulation and contributions from 75 historical and prehistorical earthquake ruptures. Black lines are faults where force double couples are applied and imbedded in a 1 km by 1 km grid. Modified from *Smith-Konter and Sandwell* (2009).

Chapter 11

Heat Flow Paradox

11.1 Heat Flow Paradox

The heat flow paradox relates the expected frictional heating on a strike-slip fault, such as the San Andreas Fault, to the measurements of surface heat flow above the fault (e.g., *Lachenbruch and Sass* (1980)). A straightforward calculation, using a reasonable coefficient of friction for the fault, predicts measurably high heat flow above the fault that is not observed. Is the lack of a heat flow anomaly evidence that faults are very weak or is the heat flow anomaly erased by hydrothermal circulation in the crust? In this chapter we develop a simple heat conduction model, following *Lachenbruch and Sass* (1980) to explore this paradox.

The seismogenic zone extends from the surface to a depth of about 12 km. According to Byerlee's law (*Byerlee*, 1978), the shear stress on the fault should be some fraction of the lithostatic stress.

$$\tau(z) = f\,(\rho_c - \rho_w)\,gz \qquad (11.1)$$

f	static coefficient of friction	~0.60
ρ_c	crustal density	2600 kg m^{-3}
ρ_w	water density	1000 kg m^{-3}
g	acceleration of gravity	9.8 m s^{-2}
D	depth of seismographic zone	12 km

per length for the Landers earthquake. Given the fault parameters above, this moment implies a potential seismic offset of 45 m and a recurrence time of 30000 years—a giant earthquake indeed!

There are only two ways to understand this dilemma:

1. Faults are somehow lubricated ($f \sim .05$), so the average stress on the fault is 10–20 times smaller than predicted by Byerlee's law. In this case, one has the difficulty of maintaining the elevation of the topography in California. For example, San Jacinto Mountain, which is less than 25 km from the San Andreas Fault, has a relief of about 3000 m, which implies stresses of 80 MPa (16 times the stress drop in an earthquake).

2. Faults are strong as predicted by Byerlee's Law. In this case, faults are always very close to failure and each earthquake relieves only a small fraction (~10%) of the tectonic stress. As we saw in the last section, this model implies a large amount of energy dissipation along the fault; friction from both aseismic creep and seismic rupture will generate heat. It has been proposed that perhaps during the earthquake, the coefficient of friction drops from 0.60 to, say, 0.05, to temporarily disable the heat generation. However, it seems that such a slippery fault would release all of the elastic energy during an earthquake (~45 m of offset). Another possibility is that heat is generated, but a large fraction of the heat is advected to the surface by circulation of water in the upper couple km of crust. The unfortunate implication of this high-stress model is that since faults are always close to failure, it will be almost impossible to predict earthquakes.

11.3 Exercises

Exercise 11.1.

(a) Provide an approximate formula for the magnitude of the shear stress that is needed to induce slip on a dry fault at 10 km depth in continental crust (density 2800 kg m^{-3}). Which parameter is least well known and what is a possible range for this parameter?

(b) Suppose the crust is saturated with water to 10 km depth. How does this change the stress magnitude?

Exercise 11.2. Derive equation 11.18.

Chapter 12

The Gravity Field of the Earth, Part 1

12.1 Introduction

Chapters 12 through 15 cover *physical geodesy*, the shape of the Earth and its gravity field. This is electrostatic theory applied to the Earth. Unlike electrostatics, geodesy is a nightmare of unusual equations, unusual notation, and confusing conventions. Here we attempt to simplify and condense *physical geodesy* by focussing on concepts that are central to the field of geodynamics and tectonics. Chapter 5 of *Geodynamics* (*Turcotte and Schubert*, 2014) covers much of this topic but at a lower mathematical level. For a much more complete discussion of potential theory applied to the Earth, we recommend the excellent book by *Blakely* (1995). Following *Blakely* (1995) and *Parker* (1973), most of the Cartesian calculations are performed in the Fourier transform domain which greatly simplyfies operations such as upward and downward continuation as well as modeling of complex density interfaces. Satellite radar altimetry has revolutionized our understanding of the gravity field, tectonics, and topography of the oceans so we focus on methods of processing and gridding these data in Chapter 15.

The things that make physical geodesy messy include:

- Earth rotation;
- latitude is measured from the equator instead of the pole;
- latitude is not the angle from the equator, but is referred to the ellipsoid;
- elevation is measured from a theoretical surface called the geoid;
- spherical harmonics are defined differently from standard usage;

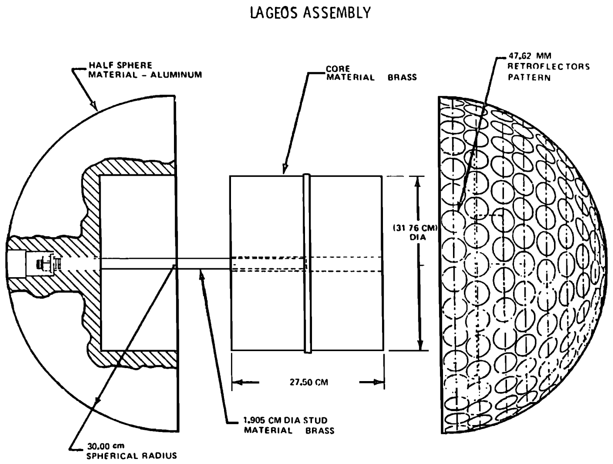

Figure 12.7: Structural detail of the LAGEOS satellite (*Cohen and Smith*, 1985).

12.3 Exercises

Exercise 12.1. Derive equation (12.6) using the ellipsoidal Earth model.

Exercise 12.2. Derive equation (12.12) by following the instructions in the paragraph preceding this equation. Assume $\frac{a}{c} \cong 1$.

Exercise 12.3. Derive equation (12.16). You may need to refer to the book by *Stacey* (1977, Chapter 4, page 76).

Exercise 12.4. A sun synchronous orbit has a prograde precession rate of once per year. This type of orbit is used by optical remote sensing satellites to have the same sun illumumination for every repeat cycle. Use equation (12.16) to calculate the inclination of the orbit plane needed to match this rate for a satellite in a circular orbit at 800 km.

Exercise 12.5. Assume the density of the Earth is uniform and the earth is a perfect sphere.

(a) Develop a formula for the gravitational acceleration as a function of radius inside the Earth and check the dimensions.

(b) Develop a formula for the pressure at the center of this Earth and check the dimensions.

Chapter 14

Laplace's Equation in Spherical Coordinates

14.1 Introduction

As discussed in Chapter 12, the gravity field of the Earth can be decomposed into a reference gravity model (e.g., WGS84), and anomalies which can be expanded in spherical harmonics and/or Fourier series. The spherical harmonic decomposition should be used for longer wavelength anomalies (i.e., $\lambda > 1000$ km). However, for shorter wavelength anomalies (e.g., $\lambda < 1000$ km), the Fourier series representation is more practical and computationally efficient.

We begin by introducing spherical harmonics and their properties. We explain how the spherical harmonic decomposition of a function on a sphere is analogous to the Fourier series decomposition of a 2-D function in Cartesian coordinates. We then use this spherical harmonic formulation to solve Laplace's equation. Finally, we describe how the Earth's gravity field is represented as spherical harmonic coefficients. This chapter follows from *Jackson* (1998, Chapter 3). However, when we apply this mathematical development to the Earth, we replace the colatitude measured from the z-axis—commonly used by mathematicians and physicists—with the geocentric latitude measured from the equator—commonly used by Earth scientists.

In summary, one can calculate the gravity field at a radius greater than the equatorial radius of the Earth. If the calculation is performed in an Earth-fixed coordinate system rotating with the Earth, then the gravity computed using the WGS84 reference model in equation (13.3) is added to the disturbing potential computed using spherical harmonic coefficients; see equation (14.18).

$$\begin{aligned} U(r,\theta,\phi) = \frac{-GM_e}{r}&\left\{1+\sum_{l=2}^{\infty}\sum_{m=0}^{m=l}\left(\frac{a}{r}\right)^l \tilde{P}_l^m(\sin\theta)\left[C_l^m\cos(m\phi)+S_l^m\sin(m\phi)\right]\right\} \\ &-\frac{1}{2}\omega^2r^2\cos^2\theta \end{aligned} \tag{14.21}$$

There is an excellent web service (`http://icgem.gfz-potsdam.de`) where one can select their favorite gravity model as spherical harmonic coefficients and then compute a wide variety of gravity products (e.g., geoid height, free-air anomaly, gravity gradient,. . .) on a grid defined by the user.

14.5 Exercises

Exercise 14.1. Show that equation 14.12 is a solution to the differential equation 14.11.

Exercise 14.2. Write a matlab program to generate Figure 14.2. Also plot the ratio of the two upward continuation functions to degree 80.

Chapter 15

Laplace's Equation in Cartesian Coordinates and Satellite Altimetry

15.1 Solution to Laplace's Equation

Variations in the gravitational potential and the gravitational force are caused by local variations in the mass distribution in the Earth. As described in Chapter 12 we decompose the gravity field of the Earth into three fields:

- the main field due to the total mass of the Earth;
- the second harmonic due to the flattening of the Earth by rotation; and
- anomalies which can be expanded in spherical harmonics or Fourier series.

Here we are interested in anomalies due to local structure. Consider a patch on the Earth having a width and length less than about 1000 km, or 1/40 of the circumference of the Earth. Within that patch, we are interested in features as small as perhaps 1 km wavelength. Using a spherical harmonic representation would require 40,000 squared coefficients! To avoid this enormous computation and still achieve accurate results, we will treat the Earth as being locally flat. Here is a remove/restore approach that has worked well in our analysis of gravity and topography:

1. Acquire a spherical harmonic model of the gravitational potential of the Earth and generate models of the relevant quantities (e.g., geoid height, gravity anomaly,

minimum distance should be about 1/4 of the shortest wavelength that one strives to resolve. When the number of knot locations is less than the number of data constraints, then the linear system is over-determined and the surface will not exactly match the slope constraints. Since we only wish to match the slopes to within the expected uncertainty of each data type, each equation equation (15.31) and (15.32) should be divided by the slope and height uncertainty to provide the optimal solution using a singular value decomposition algorithm. For recovery of the gravity field and its derivatives, we are not usually interested in the absolute height of the surface but just the local slope so our final result is the gradient of the surface. For the zero tension, biharmonic case, the gradient is

$$\nabla\phi\left(\mathbf{x}\right) = \mathbf{x}\left(2\ln|\mathbf{x}| + 1\right). \tag{15.33}$$

If we are interested in mean sea surface height (~geoid height) then equation (15.30) should be used. While this interpolation theory is elegant and very flexible, it is difficult to apply to the altimeter interpolation problem because today (2020) there are over 3 billion observations to grid. Consider gridding just 1000 slopes, the matrix of the linear system could have 10^6 elements if all the knot points were retained. In practice, we make the following compromises in order to grid this large and diverse set of data. 1) The data are residuals with respect to a model (e.g., EGM2008) so we can assemble and grid the data in overlapping small areas. 2) To avoid edge effects the sub areas have 100% overlap and only the inner interpolated cells are retained. 3) The along-track slope data from each of the 10 possible slope directions (i.e. ascending and descending profiles from 5 satellite inclinations ERS/Envisat/Altika, GEOSAT, TOPEX/Jason-1/2, Cryosat-2, and Sentinel-3) and associated uncertainties are binned onto the regularly-spaced, square grid cells (1 minute or smaller), and only the median slope of each type is retained for fitting. The results of the computations are grids of residual east and north vertical deflection that are converted to gravity anomalies and vertical gravity gradient using equations (15.12) and (15.13), respectively. Note this gridding approach is available in Generic Mapping Tools (GMT) as the function *greenspline* and also in MATLAB as the function *griddata*.

15.5 Exercises

Exercise 15.1. Use Laplace's equation and the various definitions to develop gravity anomaly from vertical deflection (equation (15.13)) and vertical gravity gradient from ocean surface curvature (equation (15.14)).

Exercise 15.2. Show that the equation (15.29) is the Green's function for the biharmonic equation by showing the following equation is true $\nabla^4|\mathbf{x}|^2\ln|\mathbf{x}| = 8\delta\left(\mathbf{x}\right)$.

Chapter 16

Poisson's Equation in Cartesian Coordinates

16.1 Solution to Poisson's Equation

As in Chapter 15 on Laplace's equation, we are interested in anomalies due to local structure and will use a flat-Earth approximation. However, unlike Chapter 15, the emphasis is on generating models of the disturbing potential and its derivatives from a 3-D model of the variations in density and topography of the Earth. In Chapter 17, we'll combine this approach to calculating gravity models with the models for isostasy and flexure, to develop a topography-to-gravity transfer function. Consider the disturbing potential

$$\underset{\substack{\text{total}\\\text{potential}}}{U} = \underset{\substack{\text{reference}\\\text{potential}}}{U_o} + \underset{\substack{\text{disturbing}\\\text{potential}}}{\Phi} \tag{16.1}$$

where, in this case, the reference potential comprises the ellipsoidal reference Earth model plus the reference spherical harmonic model. The disturbing potential satisfies Laplace's equation for an altitude z above the highest mountain in the area, while it satisfies Poisson's equation below this level, as shown in Figure 16.1.

First, consider a density model consisting of an infinitesimally thin sheet at a depth z_o having a surface-density of $\sigma(x, y)$ (units of mass per unit area). Later, we'll construct a more complicated 3-D structure from a stack of many layers. Poisson's equation is an inhomogeneous second-order partial differential equation in three dimensions

$$\frac{\partial^2 \Phi}{\partial x^2} + \frac{\partial^2 \Phi}{\partial y^2} + \frac{\partial^2 \Phi}{\partial z^2} = -4\pi G\sigma(\mathbf{x})\,\delta(z - z_o). \tag{16.2}$$

1. The free-air correction accounts for the decrease in gravity, because the observation point is farther from the center of the Earth.
2. The Bouguer correction uses the infinite-slab approximation to account for the gravitational attraction of the rock between the measurement point and the geoid. Note that unless the topography is very flat over a large area, this infinite-slab approximation may not be very accurate, and a more accurate terrain correction should be applied.

$$\underset{\substack{\text{Bouguer}\\ \text{gravity}}}{\Delta g_B} \quad = \quad \underset{\substack{\text{measured}\\ \text{gravity}}}{g_t} \quad - \quad \underset{\substack{\text{slab}\\ \text{correction}\\ \\ (-0.1118\text{ mGal/m})\\ (\rho_o = 2670\text{k}gm^{-3})}}{2\pi G\rho_o h} \quad + \quad \underset{\substack{\text{free-air}\\ \text{correction}\\ \\ (0.3086\text{ mGal/m})}}{\frac{2GM_e}{R_e^3}h} \quad - \quad \underset{\substack{\text{International}\\ \text{Gravity Formula}}}{\gamma_o(\theta)} \tag{16.24}$$

16.6 Gravity Anomaly from Topography: Parker's Exact Formula

In the previous development (Section 16.2), we collapsed the topography $t(\mathbf{x})$ into a thin sheet with varying surface density. The approximation is accurate when the amplitude of the topography is less than the upward continuation distance. For example, in the ocean where the mean seafloor depth is 4 km, the approximation works quite well for topography that extends 2 km above that depth. However, when the topography is rugged and approaches the observation plane (e.g., sea surface), a more accurate treatment is needed. *Parker* (1973) derived a more accurate formula that results in a Taylor series expansion in powers of topography.

Consider the exact formula for the disturbing potential $\Phi\left(\mathbf{x_0}, z_o\right)$ due to a uniform density slab having a flat bottom and upper surface topography $t\left(\mathbf{x}\right)$ (see Figure 16.5).

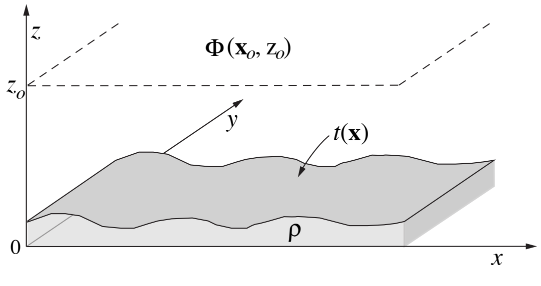

Figure 16.5

This is given by the following 3-D convolution integral

$$\Phi\left(\mathbf{x}_o, z_o\right) = \rho G \int_{-\infty}^{\infty} \int_{-\infty}^{\infty} \int_{0}^{t(\mathbf{x})} \left[(x - x_o)^2 + (y - y_o)^2 + (z - z_o)^2\right]^{-1/2} \mathrm{d}z\, \mathrm{d}^2\mathbf{x}. \tag{16.25}$$

Take the 2-D Fourier transform of the disturbing potential on the observation plane

$$\Im\left[\Phi\right] = \Phi\left(\mathbf{k}, z_o\right) =$$
$$\rho G \int_{-\infty}^{\infty} \int_{-\infty}^{\infty} \int_{0}^{t(\mathbf{x})} \int_{-\infty}^{\infty} \int_{-\infty}^{\infty} \left[(x - x_o)^2 + (y - y_o)^2 + (z - z_o)^2\right]^{-1/2} e^{-i2\pi(\mathbf{k}\cdot\mathbf{x}_o)} \mathrm{d}^2\mathbf{x}_o\, \mathrm{d}z\, \mathrm{d}^2\mathbf{x}. \tag{16.26}$$

In Section 16.3, we showed that the 2-D Fourier transform of convolution the inverse distance Green's function is given by equation (16.17):

$$\Im\left[\left(x^2 + y^2 + z^2\right)^{-1/2}\right] = \frac{e^{-2\pi|\mathbf{k}|z}}{|\mathbf{k}|}. \tag{16.27}$$

Also, recall the shift property of the Fourier transform equation (2.23):

$$\Im\left[f\left(\mathbf{x}{-}\mathbf{x}_o\right)\right] = e^{-i2\pi(\mathbf{k}\cdot\mathbf{x})} F\left(\mathbf{k}\right). \tag{16.28}$$

Using these tools, we can write the Fourier transform of the disturbing potential as

$$\Phi\left(\mathbf{k}, z_o\right) = \rho G \int_{-\infty}^{\infty} \int_{-\infty}^{\infty} \int_{0}^{t(\mathbf{x})} \frac{e^{-2\pi|k|(z_o - z)}}{|k|} e^{-i2\pi(\mathbf{k}\cdot\mathbf{x})}\, \mathrm{d}z\, \mathrm{d}^2\mathbf{x}. \tag{16.29}$$

The integral over z can be performed analytically

$$e^{-2\pi|\mathbf{k}|z_o} \int_{0}^{t(\mathbf{x})} e^{2\pi|\mathbf{k}|z} dz = \frac{e^{-2\pi|\mathbf{k}|z_o}}{2\pi\left|\mathbf{k}\right|} \left[e^{2\pi|\mathbf{k}|t(\mathbf{x})} - 1\right]. \tag{16.30}$$

We can expand the term in brackets in a Taylor series about $|\mathbf{k}| = 0$

$$\left[1 + 2\pi\left|\mathbf{k}\right| t\left(\mathbf{x}\right) + \frac{|2\pi\mathbf{k}|^2}{2!} t^2\left(\mathbf{x}\right) + \cdots - 1\right]. \tag{16.31}$$

Now we can rewrite the Fourier transform of the disturbing potential on the plane as

$$\Phi\left(\mathbf{k}, z_o\right) = 2\pi\rho G e^{-2\pi|k|z_o} \sum_{n=1}^{\infty} \frac{|2\pi\mathbf{k}|^{n-2}}{n!} \Im\left[t^n\left(\mathbf{x}\right)\right]. \tag{16.32}$$

Finally, note that the gravity anomaly is the negative vertical derivative of the potential $\Delta g = -\frac{\partial \Phi}{\partial z}$, so the result is

$$\Delta g(\mathbf{k}, z_o) = 2\pi\rho G e^{-2\pi|\mathbf{k}|z_o} \sum_{n=1}^{\infty} \frac{|2\pi\mathbf{k}|^{n-1}}{n!} \mathfrak{I}\left[t^n(\mathbf{x})\right]. \tag{16.33}$$

This exact formula for computing gravity anomaly from topography involves an infinite series of Fourier transforms of the topography raised to the power n. In the derivation of the approximate formula for gravity due to seafloor topography (Section 16.2), we compressed the topography, times the density contract across the seafloor, into surface density at an average seafloor depth. We see now that this is equivalent to keeping just the $n = 1$ term in equation (16.33) to arrive at

$$\Delta g(\mathbf{k}, z_o) = 2\pi\rho G e^{-2\pi|\mathbf{k}|z_o} T(\mathbf{k}). \tag{16.34}$$

Parker (1973) proves that this series converges as long as the highest peak in the topography does not extend above the observation plane. Moreover, the convergence of the series is optimal when the $z = 0$ level is selected such that it is half way between the maximum and minimum topography.

One can use this more exact formula for calculating gravity due to flexurally-compensated topography, as discussed in the next chapter.

16.7 Exercises

Exercise 16.1. Abyssal hills on the seafloor have a characteristic wavelength of 10 km and a peak-to-trough amplitude of 500 m.

(a) What is the amplitude of the gravity anomaly on the seafloor assuming the topography (density 2800 kg m^{-3}) can be compressed into a thin sheet?

(b) What is the amplitude of the gravity anomaly at the sea surface where the mean ocean depth is 3 km?

(c) Over a time period of 50 Ma, the abyssal hills will be carried by plate tectonics into the deep ocean where the depth is 5 km. What is the new amplitude of the gravity anomaly?

(d) In addition to a deeper ocean, the topography of the abyssal hills will be covered with sediment so the seafloor is now flat. What is the new value of the amplitude of the gravity? (Use a sediment density of 2300 kg m^{-3}.)

Exercise 16.2. Derive the Bouguer formula (equation 16.23) for the gravity due to a slab of uniform thickness H and uniform density ρ_o from the Parker expansion for gravity due to topography of uniform density (equation (16.33)). Replace $t(\mathbf{x})$ by H and continue the calculation.

Chapter 17

Gravity/Topography Transfer Function and Isostatic Geoid Anomalies

17.1 Introduction

This chapter combines thin-elastic plate flexure theory with the solution to Poisson's equation, to develop a linear relationship between gravity and topography. This relationship can be used in a variety of ways:

1. If both the topography and gravity are measured over an area that is several times greater than the flexural wavelength, then the gravity/topography relationship (in the wavenumber domain) can be used to estimate the elastic thickness of the lithosphere and/or the crustal thickness. There are many good references on this topic, including: *Dorman and Lewis* (1972); *McKenzie and Bowin* (1976); *Banks et al.* (1977); *Watts* (1978); *McNutt* (1979).

2. At wavelengths greater than the flexural wavelength, where features are isostatically compensated, the geoid/topography ratio can be used to estimate the depth of compensation of crustal plateaus and the depth of compensation of hot-spot swells (*Haxby and Turcotte*, 1978).

3. If the gravity field is known over a large area, but there is rather sparse ship-track coverage, the topography/gravity transfer function can be used to interpolate the seafloor depth among the sparse ship soundings (*Smith and Sandwell*, 1994).

17.8 Exercises

Exercise 17.1. As discussed in Chapter 2, the Fourier transform of the derivative of a function is equal to $i2\pi k$ times the Fourier transform of the original function where k is the wavenumber (1/wavelength), and i is the square root of -1. Show that this relationship also holds for a discrete time series by carrying out the operations on the computer. Use the first difference formula to compute the derivative of the geoid height profile. Also compute the derivative by multiplication in the Fourier domain. Apply a phase shift to the FFT derivative so it will be aligned with the first difference derivative. Compare results. Obtain the data at: `https://topex.ucsd.edu/pub/class/geodynamics/hw1`.

Exercise 17.2. Given the relationship between gravity anomaly and topography in the Fourier transform domain provided in equation (17.9):

(a) Plot this transfer function (i.e., $Q(|\mathbf{k}|) = \Delta g/T$) for wave numbers $|\mathbf{k}|$ ranging from 0 to 10^{-3} m^{-1}. Use elastic thicknesses of 0 m and 30000 m. Why does the transfer function approach zero at high wave numbers? Why does it approach zero at low wave numbers?

(b) Explain what happens when the elastic thickness is zero and derive the relationship between topography (above the base level) and the total crustal thickness?

(c) Using this transfer function $Q(|\mathbf{k}|)$ and the topography given in the computer file `https://topex.ucsd.edu/pub/class/geodynamics/hw6`, calculate a model gravity anomaly profile for $h = 0$. The basic procedure is to take the Fourier transform of the topography, multiply by the transfer function and inverse Fourier transform the result.

(d) Compare this model gravity profile with the observed gravity profile. Increase the elastic thickness until the model gravity profile matches the observed gravity profile. How does this value of elastic thickness compare with the value found by *Watts* (1978)? How old was the lithosphere when this seamount formed?

Exercise 17.3.

(a) Use the formula for the geoid height due to long wavelength isostatically compensated topography (equation 17.15) to calculate the geoid height due to the following density model:

$$\Delta\rho = \sigma\left[\delta(z) - \delta(z+a)\right]$$

(b) What is the change in geoid height for a topography step of 4 km, a density of 2800 kg m^{-3}, and a compensation depth a of 40 km?

(c) What is the magnitude of the outward swell push force? What is the depth-averaged stress needed to maintain this topography?

Chapter 18

Postglacial Rebound

18.1 Introduction and Dimensional Analysis

This chapter considers the classic problem of the viscous response of the mantle to rapid melting of the ice sheets following the last glacial maximum. The approach is similar to that in *Geodynamics* (*Turcotte and Schubert*, 2014, Section 6-10), but is for an arbitrary-shaped initial topography rather than a single wavelength cosine function. The initial condition is shown in Figure 18.1.

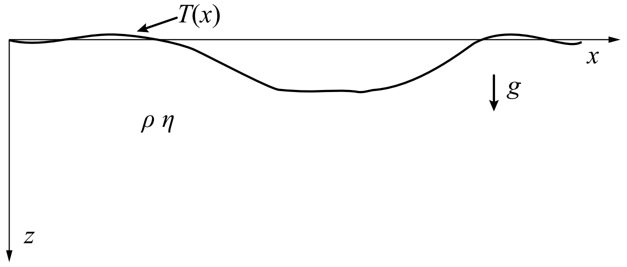

Figure 18.1: Viscous half space with an initial surface topography that decays exponentially with time under the restoring force of gravity.

18.4 Exercises

Exercise 18.1. Given the parameters in Table 18.1, develop (guess) characteristic times for the following processes:

(a) *Heat diffusion:* Describe this timescale in terms of an experiment or process.

(b) *Maxwell viscoelastic relaxation:* Describe this timescale in terms of an experiment or process.

(c) *Glacial rebound, viscosity:* Describe this timescale in terms of an experiment or process.

Parameter	Definition	Value/Unit
κ	Thermal diffusivity	$8 \times 10^{-7} \text{m}^2 \text{s}^{-1}$
h	Wine cellar depth	3 m
E	Young's modulus	6.5×10^{10} Pa
η	Dynamic viscosity	10^{20} Pa s
ρ	Mantle density	3300 kg m^{-3}
g	Acceleration of gravity	9.82 m s^{-2}
λ	Wavelength of surface deformation	3000 km

Table 18.1: Parameters needed for Exercise 18.1.

Chapter 19

Driving Forces of Plate Tectonics

19.1 Introduction

The major forces acting to drive the tectonic plates are nicely presented in the classic paper by *Forsyth and Uyeda* (1975). They are: (1) the gravitational sliding force of the cooling oceanic lithosphere also called the ridge-push force F_r; (2) the slab pull force F_s that is caused by the negative buoyancy of the cold subducted lithosphere; and (3) the viscous shear coupling τ (usually drag) on the base of the plate and both surfaces of the subducted plate (Figure 19.1). The ridge push and slab pull are body forces having units of force per length along the strike of the trench. The viscous drag is a stress having a force per area. The magnitude of the drag force depends on the ridge-to-trench plate length, the plate speed, and the viscosity. In this simple model we have an asthenosphere with a relatively low viscosity above the mesosphere having a 30-300 times higher viscosity (*Hager*, 1984). In addition to these main forces, there is a resistive force at the interface between the subducting oceanic plate and the overriding continental plate between the surface and depth of ~40 km. This is a stick-slip zone where megathrust earthquakes are generated.

There are additional body forces (Figure 19.2) associated with phase changes within the subducting lithosphere (e.g., *Arredondo and Billen* (2017)). There are three major phase transitions: (1) at a depth of about 125 km, the basalt in the crust undergoes a phase change to denser eclogite; (2) at a depth of about 410 km, the primarily endothermic phase change of olivine to spinel increases the density of the cold interior of the lithosphere which adds a significant downward body force; (3) at a depth of about 660 km, the exothermic phase changes decrease the density of the cold interior of the

These models also predict that the negative buoyancy of the slabs in the lower mantle drives deep mantle flow but at a much slower rate due to the higher viscosity (*Kohlstedt et al.*, 1995). An example of a numerical simulation of a subducting plate is shown in Figure 19.6. This 80-Ma lithosphere has subducted for 40 Ma so a large part of the slab extends into the much higher viscosity lower mantle where if folds due to the resistive viscous drag.

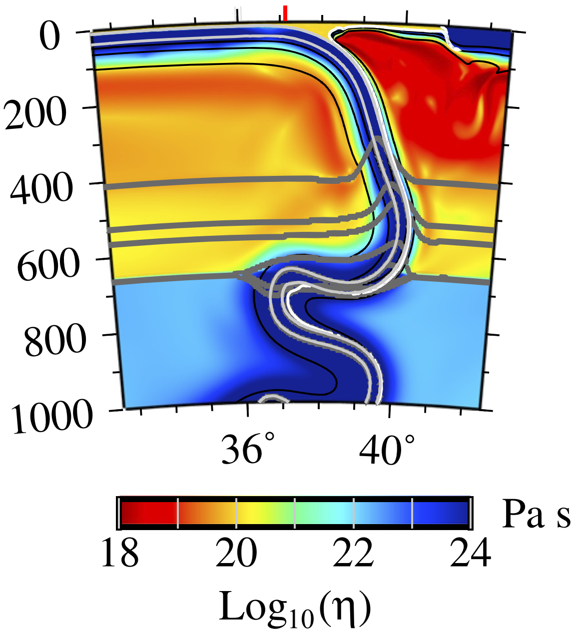

Figure 19.6: Numerical model of lithospheric subduction (*Arredondo and Billen*, 2017). Buoyancy due to phase changes (Figure 19.3) are combined with the thermal buoyancy to drive subduction. The 80-Ma lithosphere has a very high yield strength of 1000 MPa that enables the plate to remain intact. The upper mantle viscosity is 10^{19} Pa s while the lower mantle has a much higher viscosity of 10^{22} Pa s.

19.7 Exercises

Exercise 19.1. Write a program to calculate the ridge-push force versus cooling time on Venus for asympototic plate thicknesses of 125 and 500 km. Use a surface temperature of 455C and a deep mantle temperature somewhat higher than the Earth at 1400C. How does this compare with Earth?

Exercise 19.2. Write a short essay on the arguments for and against lithospheric subduction on Venus. Begin with a brief summary of the main observations that were used to confirm lithospheric subduction on the Earth. Then discuss some of the published arguments for and against subduction on Venus. End with a discussion of how to prove or disprove the subduction theory with another mission to Venus? There is an extensive reference list at the following web site `https://topex.ucsd.edu/venus/index.html`.

Exercise 19.3. Describe the three major phase changes that occur within subducting lithosphere. Explain how they affect lithospheric buoyancy. What is the Clapeyron slope?

Bibliography

Arredondo, K., and M. Billen, Coupled effects of phase transitions and rheology in 2-d dynamical models of subduction, *Journal of Geophysical Research: Solid Earth*, *122*(7), 5813–5830, 2017.

Banks, R., R. Parker, and S. Heustis, Isostatic compensation on a continental scale: Local versus regional mechanisms, *Geophys. J. R. Astr. Soc.*, *51*, 431–452, 1977.

Becker, J., et al., Global bathymetry and elevation data at 30 arc seconds resolution: SRTM30-PLUS, *Marine Geodesy*, *32*(4), 355–371, 2009.

Blakely, J., *Potential Theory in Gravity and Magnetics*, Cambridge University Press, New York, 1995.

Brace, W., and D. Kohlstedt, Limits on lithospheric stress imposed by laboratory experiments, *J. Geophys. Res.*, *85*(B11), 6248–6252, 1980.

Bracewell, R., *The Fourier Transform and Its Applications.*, second ed., McGraw-Hill Book Co., New York, 1978.

Brown, C., and R. Phillips, Flexural rift flank uplift at the Rio Grande rift, New Mexico, *Tectonics*, *18*(6), 1275–1291, 1999.

Burridge, R., and L. Knopoff, Body force equivalents for seismic dislocations, *Bulletin of the Seismological Society of America*, *54*(6A), 1875–1888, 1964.

Byerlee, J., Friction of rocks, in *Rock friction and earthquake prediction*, pp. 615–626, Springer, 1978.

Caldwell, J., W. Haxby, D. E. Karig, and D. Turcotte, On the applicability of a universal elastic trench profile, *Earth and Planetary Science Letters*, *31*(2), 239–246, 1976.

Cande, S., J. LaBrecque, R. Pitman, X. Golovchenko, and W. Haxby, *Magnetic Lineations of the World's Ocean Basins.*, American Association of Petroleum Geologists, Tulsa, OK, 1989.

Carslaw, H., and J. Jaeger, *Conduction of Heat in Solids*, second ed., Oxford University Press, Oxford, UK, 1959.

Chen, Y. J., Oceanic crustal thickness versus spreading rate, *Geophysical Research Letters*, *19*(8), 753–756, 1992.

Cohen, S., Numerical models of crustal deformation in seismic zones, *Advances in Geophysics*, *41*, 134–231, 1999.

Cohen, S., and D. Smith, Lageos scientific results: Introduction, *Journal of Geophysical Research: Solid Earth*, *90*(B11), 9217–9220, 1985.

Conrad, C., and C. Lithgow-Bertelloni, How mantle slabs drive plate tectonics, *Science*, *298*(5591), 207–209, 2002.

Crough, S., Hotspot swells, *Annual Review of Earth and Planetary Sciences*, *11*(1), 165–193, 1983.

Cuffey, K., and W. Patterson, *The physics of glaciers, ed*, Butterworth-Heinemann, imprint of Elsevier, Burlington, MA, 2010.

Dalen, F., Isostasy and the ambient state of stress in the oceanic lithosphere, *J. Geophys. Res.*, *86*, 7801–7807, 1981.

DeMets, C., R. Gordon, D. Argus, and S. Stein, Current plate motions, *Geophys. J. R. Astr. Soc.*, *101*, 425–478, 1990.

DeMets, C., R. Gordon, D. Argus, and S. Stein, Geologically current plate motions, *Geophys. J. Int.*, *181*, 1–80, 2010.

Doin, M., and L. Fleitout, Thermal evolution of the oceanic lithosphere: An alternate view, *Earth Planet. Sci. Lett.*, *142*, 121–136, 1996.

Dorman, L., and B. Lewis, Experimantal isostasy 3: Inversion of the isostatic Green's function and lateral density changes, *J. Geophys. Res.*, *77*, 3068–3077, 1972.

Engdahl, E., R. VanderHilst, and R. Buland, Global teleseismic earthquake relocation with improved travel times and procedures for depth determination., *IBull. Seismo. Soc. Am.*, *88*, 722–743, 1998.

Fialko, Y., Temperature fields generated by the elastodynamic propagation of shear cracks in the earth, *Journal of Geophysical Research: Solid Earth*, *109*(B1), 2004.

Fleitout, L., and C. Froidevaux, Tectonics and topography for a lithosphere containing density heterogeneities, *Tectonics*, *1*, 21–56, 1982.

Fleitout, L., and C. Froidevaux, Tectonic stresses in the lithosphere, *Tectonics*, *2*, 315–324, 1983.

Flesch, L., A. Haines, and W. Holt, Dynamics of the India-Eurasia collision zone, *Journal of Geophysical Research: Solid Earth*, *106*(B8), 16,435–16,460, 2001.

Forsyth, D., and S. Uyeda, On the relative importance of the driving forces of plate motion, *Geophysical Journal International*, *43*(1), 163–200, 1975.

Fowler, C., *The Solid Earth: An Introduction to Global Geophysics*, Cambridge University Press, Cambridge, MA, 1990.

Garcia, E., D. Sandwell, and K. Luttrell, An iterative spectral solution method for thin elastic plate flexure with variable rigidity, *Geophysical Journal International*, *200*(2), 1012–1028, 2014.

Garcia, E., D. Sandwell, and D. Bassett, Outer trench slope flexure and faulting at Pacific basin subduction zones, *Geophysical Journal International*, *218*(1), 708–728, 2019.

Garland, G., *The Earth's Shape and Gravity*, Permagon Press, 1977.

Gee, J., and D. Kent, Variation in layer 2A thickness and the origin of the central anomaly magnetic high, *Geophys. Res., Lett.*, *21*(4), 297–300, 1994.

Goetze, C., and B. Evans, Stress and temperature in the bending lithosphere as constrained by experimental rock mechanics, *Geophysical Journal International*, *59*(3), 463–478, 1979.

Greenberg, M., *Applications of Green's functions in science and engineering*, Courier Dover Publications, 2015.

Hager, B., Subducted slabs and the geoid: Constraints on mantle rheology and flow, *Journal of Geophysical Research: Solid Earth*, *89*(B7), 6003–6015, 1984.

Hasterok, D., A heat flow based cooling model for tectonic plates, *Earth and Planetary Science Letters*, *361*, 34–43, 2013.

Haxby, W., and D. Turcotte, On isostatic geoid anomalies, *J. Geophys. Res.*, *83*, 5,473–5,478, 1978.

Haxby, W., G. Garner, J. LaBrecque, and J. Weissel, Digital images of combined oceanic and continental data sets and their use in tectonic studies., *EOS Trans. Amer. Geophys. Un.*, *64*, 995–1004, 1983.

Horner-Johnson, B. C., and R. Gordon, Equatorial Pacific magnetic anomalies identified from vector aeromagnetic data, *Geophysical Journal International*, *155*(2), 547–556, 2003.

Hwang, C., and B. Parsons, An optimal procedure for deriving marine gravity from multi-satellite altimetry., *J. Geophys. Int.*, *125*, 705–719, 1996.

Jackson, J., *Classical Electrodynamics*, third ed., John Wiley & Sons, New York, 1998.

Jaeger, J., N. Cook, and R. Zimmerman, *Fundamentals of rock mechanics*, John Wiley & Sons, 2009.

Johnson, C., and D. Sandwell, Lithospheric flexure on Venus, *Geophysical Journal International*, *119*(2), 627–647, 1994.

Kent, G., A. Harding, and J. Orcutt, Distribution of magma beneath the East Pacific rise between the Clipperton Transform and the 9° 17' deval from forward modeling of common depth point data, *J. Geophys. Res.*, *98*, 13,945–13,969, 1993.

Kohlstedt, D., B. Evans, and S. Mackwell, Strength of the lithosphere: Constraints imposed by laboratory experiments, *Journal of Geophysical Research: Solid Earth*, *100*(B9), 17,587–17,602, 1995.

Lachenbruch, A., and J. Sass, Heat flow and energetics of the San Andreas fault zone, *J. Geophys. Res.*, *85*, 6185–6222, 1980.

Laske, G., G. Masters, Z. Ma, and M. Pasyanos, Update on CRUST1.0 A 1-degree global model of Earthrs crust, in *Geophys. Res. Abstr*, vol. 15, p. 2658, EGU General Assembly Vienna, Austria, 2013.

Leeds, A., and E. Kausel, Variations of upper mantle structure under the Pacific Ocean., *Science*, *186*, 141–143, 1974.

Levitt, D., and D. Sandwell, Lithospheric bending at subduction zones based on depth soundings and satellite gravity, *J. Geophys. Res.: Solid Earth*, *100*, 379–400, 1995.

Luttrell, K., D. Sandwell, B. Smith-Konter, B. Bills, and Y. Bock, Modulation of the earthquake cycle at the southern San Andreas fault by lake loading, *Journal of Geophysical Research: Solid Earth*, *112*(B8), 2007.

Massell, C., Large Scale Structural Variation of Trench Outer Slopes and Rises, Ph.D. dissertation, Scripps Inst. of Oceanography, La Jolla, CA, 2002.

McKenzie, D., and C. Bowin, The relationship between bathymetry and gravity in the Atlantic Ocean, *J. Geophys. Res.*, *81*, 1903–1915, 1976.

McNutt, M., Compensation of oceanic topography: An application of the response function technique to the Surveyor area, *J. Geophys. Res.*, *84*, 7,589–7,598, 1979.

McNutt, M., and H. Menard, Lithospheric flexure and uplifted atolls, *Journal of Geophysical Research: Solid Earth*, *83*(B3), 1206–1212, 1978.

McNutt, M., and H. Menard, Constraints on yield strength in the oceanic lithosphere derived from observations of flexure, *Geophs. J. R. astr. Soc.*, *71*, 363–394, 1982.

Menard, H., *Marine geology of the Pacific*, 1964.

Miller, L., and B. C. Douglas, On the rate and causes of twentieth century sea-level rise, *Philosophical Transactions of the Royal Society of London A: Mathematical, Physical and Engineering Sciences*, *364*(1841), 805–820, 2006.

Minster, J., and T. Jordan, Present-day plate motions, *J. Geophys. Res.*, *85*, 5331–5354, 1978.

Mitrovica, J. X., N. Gomez, and P. U. Clark, The sea-level fingerprint of West Antarctic collapse, *Science*, *323*(5915), 753–753, 2009.

Mueller, S., and R. J. Phillips, On the reliability of lithospheric constraints derived from models of outer-rise flexure, *Geophysical Journal International*, *123*(3), 887–902, 1995.

Müller, R., W. Roest, J. Royer, L. Gahagan, et al., Digital isochrons of the world's ocean floor, *J. Geophys. Res.*, *102*, 3211–3214, 1997.

Oxburgh, E., and E. Parmentier, Compositional and density stratification in oceanic lithosphere-causes and consequences, *Journal of the Geological Society*, *133*(4), 343–355, 1977.

Parker, R., The rapid calculation of potential anomalies, *Geophys. J. Roy. Astr. Soc.*, *31*, 441–455, 1973.

Parsons, B., and F. Richter, A relationship between the driving force and geoid anomaly associated with mid-ocean ridges, *Earth Planet. Sci. Lett.*, *51*, 445–450, 1980.

Parsons, B., and J. Sclater, An analysis of the variation of the ocean floor bathymetry and heat flow with age, *J. Geophys. Res.*, *82*, 803–827, 1977.

Pavlis, N., S. Holmes, S. Kenyon, and J. Factor, The development and evaluation of the Earth Gravitational Model 2008 (EGM2008), *J. Geophys. Res.*, *117*(B4), 2012.

Priestley, K., D. McKenzie, and T. Ho, A lithosphere–asthenosphere boundarya global model derived from multimode surface-wave tomography and petrology, *Lithospheric discontinuities*, pp. 111–123, 2018.

Rapp, R., and Y. Yi, Role of ocean variability and dynamic topography in the recovery of the mean sea surface and gravity anomalies from satellite altimeter data., *J. Geodesy*, *71*, 617–629, 1997.

Renkin, M., and J. Sclater, Depth and age in the North Pacific, *Journal of Geophysical Research-Solid Earth and Planets.*, *93*, 2919–2935, 1988.

Ryan, M. (Ed.), *Magmatic Systems*, Academic Press, San Diego, 1994.

Sandwell, D., Thermal isostasy: response of a moving lithosphere to a distributed heat source, *J. Geophys. Res.*, *87*, 1001–1014, 1982a.

Sandwell, D., Thermal isostasy: Response of a moving lithosphere to a distributed heat source, *Journal of Geophysical Research: Solid Earth*, *87*(B2), 1001–1014, 1982b.

Sandwell, D., Thermomechanical evolution of oceanic fracture zones, *J. Geophys. Res.*, *89*, 11,401–11,413, 1984.

Sandwell, D., Biharmonic spline interpolation of geos-3 and seasat altimeter data, *Geophysical research letters*, *14*(2), 139–142, 1987.

Sandwell, D., and G. Schubert, Lithospheric flexure at fracture zones, *J. Geophys. Res.*, *87*, 4657–4667, doi:10.1029/JB087iB06p04657, 1982a.

Sandwell, D., and G. Schubert, Evidence for retrograde lithospheric subduction on Venus, *Science*, *257*(5071), 766–770, 1992.

Sandwell, D., and W. Smith, Marine gravity anomaly from Geosat and ERS-1 satellite altimetry., *J. Geophys. Res.*, *102*, 10,039–10,054, 1997.

Sandwell, D., R. D. Müller, W. Smith, E. Garcia, and R. Francis, New global marine gravity model from CryoSat-2 and Jason-1 reveals buried tectonic structure, *Science*, *346*(6205), 65–67, 2014.

Sandwell, D., H. Harper, B. Tozer, and W. Smith, Gravity field recovery from geodetic altimeter missions, *Advances in Space Research*, 2019.

Sandwell, D. T., and G. Schubert, Geoid height-age relation from seasat altimeter profiles across the Mendocino fracture zone, *J. Geophys. Res.*, *87*(B5), 3949–3958, 1982b.

Savage, J., Equivalent strike-slip cycles in half-space and lithosphere-asthenosphere earth models, *J. Geophys. Res.*, *95*, 4873–4879, 1990.

Savage, J., and R. Burford, Geodetic determination of relative plate motion in central California, *Journal of Geophysical Research*, *78*(5), 832–845, 1973.

Scambos, T., O. Sergienko, A. Sargent, D. MacAyeal, and J. Fastook, Icesat profiles of tabular iceberg margins and iceberg breakup at low latitudes, *Geophysical Research Letters*, *32*(23), 2005.

Schouten, H., and K. McCamy, Filtering marine magnetic anomalies, *J. Geophys. Res.*, *77*, 7,089–7,099, 1972.

Schouten, J. A., A fundamental analysis of magnetic anomalies over oceanic ridges, *Marine Geophysical Researches*, *1*(2), 111–144, 1971.

Schubert, G., and D. Sandwell, Crustal volumes of the continents and of oceanic and continental submarine plateaus, *Earth and Planetary Science Letters*, *92*(2), 234–246, 1989.

Schubert, G., and D. Sandwell, A global survey of possible subduction sites on Venus, *Icarus*, *117*(1), 173–196, 1995.

Sclater, J., C. Jaupart, and D. Galson, The heat flow through oceanic and continental crust and the heat loss of the Earth., *Reviews of Geophys. and Space Physics*, *18*, 269–311, 1980.

Segall, P., *Earthquake and volcano deformation*, Princeton University Press, 2010.

Seton, M., R. D. Müller, S. Zahirovic, S. Williams, N. M. Wright, J. Cannon, J. M. Whittaker, K. J. Matthews, and R. McGirr, A global data set of present-day oceanic crustal age and seafloor spreading parameters, *Geochemistry, Geophysics, Geosystems*, *21*(10), e2020GC009,214, 2020.

Siebert, L., and T. Simkin, *Volcanoes of the World: an Illustrated Catalog of Holocene Volcanoes and their Eruptions.*, vol. GVP-3, Smithsonian Institution, Global Volcanism Program, Digital Information Series, http://www.volcano.si.edu/world/, 2002.

Smith, B., and D. Sandwell, Coulomb stress accumulation along the San Andreas fault system, *Journal of Geophysical Research: Solid Earth*, *108*(B6), 2003.

Smith, B., and D. Sandwell, A three-dimensional semianalytic viscoelastic model for time-dependent analyses of the earthquake cycle, *Journal of Geophysical Research: Solid Earth*, *109*(B12), 2004.

Smith, G., and S. Banerjee, Magnetic structure of the upper kilometer of the marine crust at DSDP hole 504B, Eastern Pacific Ocean, *J. Geophys. Res.*, *91*, 10,337–10,354, 1986.

Smith, W., and D. Sandwell, Bathymetric prediction from dense satellite altimetry and sparse shipboard bathymetry, *J. Geophys. Res.*, *99*, 21,803–21,824, 1994.

Smith, W., and D. Sandwell, Global sea floor topography from satellite altimetry and ship depth soundings, *Science*, *277*, 1956–1962, 1997.

Smith-Konter, B., and D. Sandwell, Stress evolution of the San Andreas fault system: Recurrence interval versus locking depth, *Geophysical Research Letters*, *36*(13), 2009.

Stacey, F., *Physics of the Earth*, John Wiley & Sons, 1977.

Staudigel, H., A. Koppers, J. Lavelle, T. Pitcher, and T. Shank, Defining the word ”seamount”, *Oceanography*, *23*(1), 2010.

Stein, C. A., and S. Stein, A model for the global variation in oceanic depth and heat flow with lithospheric age, *Nature*, *359*(6391), 123–129, 1992.

Steketee, J., On Volterra’s dislocations in a semi-infinite elastic medium, *Canadian Journal of Physics*, *36*(2), 192–205, 1958.

Tozer, B., D. Sandwell, W. Smith, C. Olson, J. Beale, and P. Wessel, Global bathymetry and topography at 15 arc sec: Srtm15+, *Earth and Space Science*, *6*(10), 1847–1864, 2019.

Turcotte, D., and E. Oxburgh, Finite amplitude convection cells and continental drift, *J. Fluid Mech.*, *28*, 29–42, 1967.

Turcotte, D., and G. Schubert, *Geodynamics*, third ed., Cambridge University Press, cambridge, UK, 2014.

Van Avendonk, H. J., J. K. Davis, J. L. Harding, and L. A. Lawver, Decrease in oceanic crustal thickness since the breakup of pangaea, *Nature Geoscience*, *10*(1), 58–61, 2017.

Vaughan, D., Tidal flexure at ice shelf margins, *Journal of Geophysical Research: Solid Earth*, *100*(B4), 6213–6224, 1995.

Vink, G., W. Morgan, and W.-L. Zhao, Preferential rifting of continents: a source of displaced terranes, *J. Geophys. Res.*, *89*(B12), 10,072–10,076, 1984.

Watts, A., An analysis of isostasy in the world's oceans 1. Hawaiian-Emperor seamount chain, *J. Geophys. Res.*, *83*(B12), 5989–6004, 1978.

Watts, A., *Isostasy and Flexure of the Lithosphere*, Cambridge University Press, 2001.

Wdowinski, S., B. Smith-Konter, Y. Bock, and D. Sandwell, Diffuse interseismic deformation across the Pacific–North America plate boundary, *Geology*, *35*(4), 311–314, 2007.

Weertman, J., and J. R. Weertman, *Elementary dislocation theory*, Macmillan, 1966.

Weissel, J., and G. Karner, Flexural uplift of rift flanks due to mechanical unloading of the lithosphere during extension, *Journal of Geophysical Research: Solid Earth*, *94*(B10), 13,919–13,950, 1989.

Wessel, P., Global distribution of seamounts inferred from gridded Geosat/ERS-1 altimetry, *Journal of Geophysical Research: Solid Earth*, *106*(B9), 19,431–19,441, 2001.

Wessel, P., and D. Bercovici, Interpolation with splines in tension: a Green's function approach, *Mathematical Geology*, *30*(1), 77–93, 1998.

Wessel, P., and W. Smith, New version of the Generic Mapping Tools released, *EOS Trans. AGU*, *76*, 329, http://gmt.soest.hawaii.edu/, 1995.

Wessel, P., J. Luis, L. Uieda, R. Scharroo, F. Wobbe, W. Smith, and D. Tian, The generic mapping tools version 6, *Geochemistry, Geophysics, Geosystems*, 2019.

Index